ICARUS **124,** 113–133 (1996)
ARTICLE NO. 0193

Radar Observations of Asteroids 1 Ceres, 2 Pallas, and 4 Vesta[1]

David L. Mitchell and Steven J. Ostro

Jet Propulsion Laboratory, California Institute of Technology, Pasadena, California 91109
E-mail: mitchell@think.jpl.nasa.gov

R. Scott Hudson

School of Electrical Engineering and Computer Science, Washington State University, Pullman, Washington 99164

Keith D. Rosema

Jet Propulsion Laboratory, California Institute of Technology, Pasadena, California 91109

Donald B. Campbell

National Astronomy and Ionosphere Center, Cornell University, Ithaca, New York 14853

Reinaldo Vélez

Arecibo Observatory, Box 995, Arecibo, Puerto Rico 00613

John F. Chandler and Irwin I. Shapiro

Harvard–Smithsonian Center for Astrophysics, Cambridge, Massachusetts 02138

and

Jon D. Giorgini and Donald K. Yeomans

Jet Propulsion Laboratory, California Institute of Technology, Pasadena, California 91109

Received December 18, 1995; revised March 28, 1996

Asteroids 1 Ceres, 2 Pallas, and 4 Vesta were observed with the 13-cm Arecibo radar and the 3.5-cm Goldstone radar during several apparitions between 1981 and 1995. These observations help to characterize the objects' surface properties. Echoes from Ceres and Pallas are ~95% polarized ($\mu_C = \sigma_{SC}/\sigma_{OC} \approx 0.05$) in the sense expected for specular (mirror) reflection yet broadly distributed in Doppler frequency, thus revealing surfaces that are smoother than the Moon at decimeter scales but much rougher (rms slopes > 20°) on larger scales. Slopes on Ceres appear to be somewhat higher when viewed with the 3.5-cm wavelength, a trend that is observed for the terrestrial planets and the Moon. In contrast, echoes from Vesta are significantly depolarized, indicating substantial near-surface complexity at scales near 13 cm ($\mu_C = 0.24 \pm 0.04$) and 3.5 cm ($\mu_C = 0.32 \pm 0.04$), which is probably a consequence of Vesta's relatively strong basaltic surface material and may be a signature of large impact features inferred to be present on the surface.

The low radar albedos of Ceres ($\hat{\sigma}_{OC} = 0.042 \pm 0.006$) and Pallas ($\hat{\sigma}_{OC} = 0.075 \pm 0.011$) are in the range expected for surfaces with a carbonaceous chondrite mineralogy. Pallas' distinctly higher albedo implies a ~35% higher surface density, which could result from a lower regolith porosity and/or a higher specific gravity (zero-porosity density). Given a porosity of 45%, the specific gravities of the surface materials on Ceres and Pallas would be ~2.3 and ~3.0 g cm^{-3}, respectively, which would be consistent with (1) the presence of an additional silicate component on Pallas' surface (as inferred from spectroscopic observations) and (2) recent mass estimates, which suggest a higher mean (volume-averaged) density for Pallas than for Ceres.

1. INTRODUCTION

As end members of the asteroid size distribution, Ceres, Pallas, and Vesta strongly influence theories of the origin

[1] The U.S. Government's right to retain a nonexclusive royalty-free license in and to the copyright covering this paper, for governmental purposes, is acknowledged.

0019-1035/96 $18.00

of main-belt asteroids and their thermal and collisional evolution. The surfaces of Ceres and Pallas are believed to have a carbonaceous chondrite mineralogy that was subjected to aqueous alteration (Feierberg *et al.* 1981, Lebofsky *et al.* 1981, Larson *et al.* 1983), revealing information about thermal conditions in the early Solar System (Jones *et al.* 1990). Vesta may possess the only intact basaltic crust in the main belt, an important constraint on collisional theories (Davis *et al.* 1985), and is believed to be a source of basaltic achondrite meteorites. This last hypothesis was recently bolstered by Binzel and Xu's (1993) discovery of a population of small asteroids sharing Vesta's spectral signature and forming a dynamical link between Vesta's orbit and the 3:1 Jupiter resonance, a likely main-belt source region for Earth-crossing asteroids.

Ceres, Pallas, and Vesta have been part of an ongoing radar observing program that has now spanned more than two decades and resulted in the detection of ~70 main-belt asteroids (MBAs) and Earth-orbit-crossing asteroids (ECAs) (Ostro 1993). Ceres was the first main-belt object to be detected by radar (Ostro *et al.* 1979), and Vesta was detected two years later (Ostro *et al.* 1980). Since then, all three objects have been observed with the Arecibo 13-cm radar for multiple apparitions. In addition, the Goldstone 3.5-cm radar was used to observe Vesta in 1992 and Ceres in 1995. Initial results from Arecibo observations of 20 MBAs (Ostro *et al.* 1985, henceforth OCS85) revealed the very low radar albedo of Ceres and the extreme decimeter-scale smoothness of both Ceres and Pallas. At the other extreme, Vesta was inferred to possess substantial decimeter-scale, near-surface roughness.

From an experimental point of view, Ceres, Pallas, and Vesta plays a special role in asteroid radar astronomy because of their relatively well-determined shapes and sizes. Whereas delay-Doppler images of closely approaching ECAs have been used to constrain both target shape and radar scattering properties (Hudson 1993, Hudson and Ostro 1994, 1995), MBA observations have been limited by the echo's dependence on the fourth power of distance and by the sensitivity of available telescopes, and almost all existing MBA echoes are resolved only in Doppler frequency. Without the geometric leverage provided by delay resolution, Doppler spectra depend in a "coupled" way on size, spin vector, and scattering law. Fortunately, extensive nonradar information on the sizes, shapes, and poles of Ceres, Pallas, and Vesta provide sufficient geometric leverage to permit us to study the scattering properties of each target's surface using Doppler-only spectra.

In this paper we present detailed analyses of all radar observations of Ceres, Pallas, and Vesta conducted at Arecibo and Goldstone during 1981–1995. In the next section we describe our observations and data reduction. In Section 3 we assess nonradar information about size, shape, and spin, and in Section 4 we describe our use of radar scattering laws to infer surface properties. In Section 5 we combine the results of the previous two sections and use our echoes to constrain the surface properties of each target. In Section 6 we discuss the implications of these models on the overall understanding of Ceres, Pallas, and Vesta. We conclude by describing immediate prospects for observations of these objects with the upgraded Arecibo radar.

2. RADAR OBSERVATIONS AND DATA REDUCTION

Observational and data reduction techniques were similar to those described by Mitchell *et al.* (1995). For each "run" we transmitted a circularly polarized signal toward the target for a duration close to the round-trip echo time delay (RTT), between 22 and 36 minutes for our observations, and received echoes for a similar duration. Arecibo data were blocked into ~4-min sums, except for the 1982 Pallas and the 1981 Vesta data, which were blocked into runs. Goldstone data were blocked into 2-min sums.

Table I lists first and last observation dates, total number of runs, and average values of right ascension, declination, and distance for each apparition. The post-1981 observations used a two-channel receiving system for simultaneous recording of echoes in the same sense of circular polarization as transmitted (the SC sense) and in the opposite (OC) sense. The 1981 Vesta observations used a single-channel system, which for five runs was switched between OC and SC in alternate 4-min integrations and for another five runs was configured to receive only the OC echo. Typically, several runs were obtained each day over a span of several days to provide spectra at different asteroid rotation phases and to increase the total signal-to-noise ratio (SNR). For each radar apparition, the target's plane-of-sky motion was very small.

Echo power is given by $P_R = P_T G_T G_R \lambda^2 \sigma / (4\pi)^3 R^4$, where P_T is the transmitted power, G_T and G_R are the antenna gains during transmission and reception, λ is the wavelength, R is the radar–target distance, and σ is the radar cross section in a specified polarization, defined as 4π times the backscattered power per steradian per unit incident flux at the target. The ratio of the two cross sections defines the circular polarization ratio: $\mu_C = \sigma_{SC}/\sigma_{OC}$, a measure of the near-surface structural complexity, or "roughness," at scales near the wavelength.

We removed the mean background from each spectrum (see Ostro *et al.* 1992) and normalized the result to the standard deviation of the receiver noise power, which obeys Gaussian statistics. Uncertainties in estimates of radar cross section are due primarily to systematic errors in antenna pointing and/or calibration of antenna gain. Experience during the 1980s with observations of a variety of radar targets has led us to believe that for the most part, the absolute uncertainty in radar cross section estimates is between 20 and 50%, while relative uncertainties are half as large. For μ_c, most systematic effects cancel, and statistical uncertainty from the propagation of receiver

TABLE I
Observations

Target	Dates Spanned (UT)	Observatory	# runs	RA (h)	Dec (deg)	Dist (AU)	f_{TX} (MHz)	Δf (Hz)
1 Ceres	1984 Oct 25 – Oct 30	Arecibo	9	3.4 (0.07)	9 (0.1)	1.86 (0.023)	2380	18.8
	1986 Feb 21 – Feb 24	Arecibo	8	11.2 (0.04)	23 (0.4)	1.59 (0.004)	2380	18.8
	1990 Jan 14 – Jan 15	Arecibo	4	5.5 (0.01)	27 (0.04)	1.75 (0.006)	2380	18.8
	1995 Feb 5 – Feb 14	Goldstone	15	9.3 (0.14)	30 (0.9)	1.60 (0.015)	8510	97.7
2 Pallas	1982 Mar 21 – Mar 31	Arecibo	19	13.4 (0.11)	12 (3.5)	1.48 (0.010)	2380	18.8
	1987 Apr 4 – Apr 8	Arecibo	9	16.4 (0.01)	18 (1.0)	2.12 (0.018)	2380	18.8
	1991 Apr 20 – Apr 27	Arecibo	12	10.6 (0.04)	13 (1.4)	1.60 (0.089)	2380	18.8
4 Vesta	1981 Feb 24 – Mar 2	Arecibo	10	10.5 (0.01)	20 (0.7)	1.40 (0.002)	2380	19.5
	1988 Jan 17 – Jan 19	Arecibo	7	8.4 (0.04)	23 (0.2)	1.52 (0.004)	2380	18.8
	1992 Mar 4 – Mar 5	Arecibo	5	11.7 (0.02)	14 (0.1)	1.35 (0.003)	2380	18.8
	1992 Mar 24 – Mar 26	Goldstone	28	11.4 (0.03)	16 (0.3)	1.36 (0.007)	8510	97.7

Note. Right ascension, declination, and distance are given for epochs near the weighted midpoint of observation; the range of values spanned is in parentheses. The number of transmit–receive cycles, or runs, is given in the fourth column. (For 5 of the 10 Vesta runs in 1981, we received only the OC polarization.) The transmitter frequency (f_{TX}) and the raw frequency resolution (Δf) of the echo Doppler spectra are given in the last two columns.

noise (Appendix of Ostro *et al.* 1992) dominates our quoted errors.

Echo power was measured as a function of frequency relative to the Doppler frequency of hypothetical echoes from the center of mass (COM) as predicted by site ephemerides. The uncertainties in the Doppler-prediction ephemerides for our targets were small compared with the data's frequency resolution. An echo's instantaneous edge-to-edge bandwidth B at rotation phase ϕ can be written

$$B(\phi, \delta) = \frac{4\pi D(\phi)}{\lambda P} \cos(\delta), \tag{1}$$

where D is the breadth normal to the radar line of sight of the asteroid's pole-on silhouette, δ is the target-centered declination of the radar (the "subradar latitude"), and P is the apparent rotation period. Each target's rotation period is known quite well (Lagerkvist *et al.* 1989 and references therein) and the contribution of plane-of-sky motion to the apparent rotation was negligible for all our observations. Our ability to discern the spectral edges of an echo depends on the shape and radar scattering properties of the target and on the SNR, which for the targets discussed here is not very high. In any event, the observed bandwidth can never be greater than the maximum bandwidth, $B_{max}(\delta) = [4\pi D_{max}/\lambda P]\cos\delta$, corresponding to the maximum breadth of the target's pole-on silhouette.

3. SIZES, SHAPES, AND POLE DIRECTIONS

In this section, we assess the available information on size, shape, and pole direction for all three targets based on analyses of multiapparition lightcurves, occultations, and/or images obtained by adaptive optics and speckle techniques. This information, which is summarized in Table II, yields predictions for the subradar latitude, projected area, and edge-to-edge bandwidth during each radar apparition.

1 Ceres

Ceres' lightcurve amplitude is small (0.04 mag.) and practically independent of the asteroid's ecliptic longitude (Lagerkvist *et al.* 1987, 1988), suggesting a nearly axisymmetric shape and a small obliquity (Tedesco *et al.* 1983). Occultation observations of Ceres in 1984 yielded an elliptical silhouette with dimensions of 959 ± 5 × 907 ± 9 km (Millis *et al.* 1987). If Ceres' obliquity is zero, the sub-Earth latitude during that occultation was within 3° of Ceres' equator. Millis *et al.* assumed a spheroidal shape with equatorial and polar dimensions given by the occultation ellipse and showed that Ceres' oblateness would be very close to that expected for a homogeneous, rotationally distorted equilibrium figure.

Thermal emission from Ceres was imaged using adaptive-optics techniques at infrared wavelengths (Saint Pé *et al.* 1993). By considering the location of the warmest spot on the disk, those authors determined the pole's ecliptic coordinates to be $\lambda = 332 \pm 5°$ and $\beta = +70 \pm 15°$, corresponding to an obliquity of 10°. (The orbit of Ceres is inclined 10° relative to the ecliptic and the longitude of the ascending node is 80°.) That pole direction yields a sub-Earth latitude within 8° of Ceres' equator during the 1984 occultation, in accord with the analysis of Millis *et al.* (1987). In consideration of all this information, we adopt

TABLE II
Prior Information

Target	(1) Class	(2) Model Ellipsoid 2a	2b	2c	(3) Synodic Period	(4) Pole Direction long.	lat.	(5) Year	(6) δ	(7) $\langle A_P \rangle$	(8) B_{max} (δ)
1 Ceres	G	959 ± 21	959 ± 21	907 ± 9	9.075	332 ± 5	+70 ± 15	1984	+5 ± 7	6.834 ± 0.171	2810 – 2990
								1986	+3 ± 15	6.832 ± 0.171	2730 – 2990
								1990	+4 ± 7	6.833 ± 0.171	2820 – 2990
								1995*	+5 ± 15	6.834 ± 0.171	9630 – 10,660
2 Pallas	B	574 ± 10	526 ± 3	501 ± 2	7.811	220 ± 10	+15 ± 10	1982	−65 ± 13	2.335 ± 0.055	416 – 1280
		(prograde model)						1987	−60 ± 13	2.321 ± 0.060	585 – 1410
								1991	−26 ± 10	2.205 ± 0.052	1620 – 1990
		583 ± 18	527 ± 3	409 ± 52	7.811	71 ± 10	−19 ± 10	1982	+36 ± 12	1.989 ± 0.130	1340 – 1950
		(retrograde model)						1987	+68 ± 13	2.336 ± 0.048	314 – 1220
								1991	−3 ± 11	1.786 ± 0.208	1940 – 2130
4 Vesta	V	555 ± 25	522 ± 18	463 ± 10	5.342	334 ± 14	+56 ± 14	1981	+25 ± 15	2.020 ± 0.137	2110 – 2960
								1988	+25 ± 17	2.020 ± 0.144	2040 – 2980
								1992	+22 ± 16	2.007 ± 0.138	2170 – 2990
								1992*	+22 ± 15	2.007 ± 0.135	7850 – 10,670

(1) Taxonomic classification (Tholen 1989) based on visual and infrared data.
(2) Adopted axis dimensions (in km) of triaxial ellipsoid shape approximations for Ceres (Millis *et al.* 1987), Pallas (prograde model: Dunham *et al.* 1990, retrograde model: Drummond and Cocke 1989), and Vesta (McCarthy *et al.* 1994). The uncertainties in the *a* and *b* axes for Ceres have been increased to account for possible deviation from an oblate spheroid as suggested by the object's small but nonzero lightcurve amplitude. See Table III for additional estimates of Pallas' dimensions.
(3) Synodic periods (in hours) are from Lagerkvist *et al.* (1989) and references therein. See also Lagerkvist *et al.* (1987, 1988).
(4) Ecliptic coordinates (in degrees, B1950) of the spin vector for Ceres (Saint-Pé *et al.* 1993), Pallas (prograde solution: Binzel 1984, retrograde solution: Drummond and Cocke 1989), and Vesta (McCarthy *et al.* 1994). Alternative pole directions, which may differ from those listed, are noted in the text. See Table III for a summary of pole solutions for Pallas.
(5) Year of radar observation. Goldstone observations are identified by an asterisk.
(6) Subradar latitude over the duration of observation corresponding to the listed pole direction and its uncertainties.
(7) Unweighted average projected area (in 10^5 km^2) of the model ellipsoid over all rotation phases for the duration of observation. The uncertainty in the model's projected area incorporates the uncertainties in the axis dimensions and pole direction.
(8) Interval estimate for the maximum edge-to-edge bandwidth (in Hz) over the duration of observation for the a priori ellipsoid with the listed pole direction and synodic spin period and all associated uncertainties.

an oblate spheroid with $2a = 2b = 959 \pm 21$ km and $2c = 907 \pm 9$ km and with a pole direction of $\lambda = 332 \pm 5°$ and $\beta = +70 \pm 15°$ as an a priori model for Ceres. The stated uncertainty in the equatorial diameter allows for possible deviation from a spheroidal shape based on the asteroid's small but nonzero lightcurve amplitude.

2 Pallas

Extensive lightcurve observations (Lagerkvist *et al.* 1987, 1988, and references therein), speckle imaging (Drummond and Hege 1988), and two stellar occultations, one in 1978 (Wasserman *et al.* 1979) and a very densely observed event in 1983 (Dunham *et al.* 1990), have been analyzed by a number of investigators to estimate Pallas' shape and pole direction. Their results are summarized in Table III. There is no clear consensus in the shape estimates, but most cluster around the solution of Dunham *et al.* (1990). Similarly, most pole direction estimates cluster in two regions: one prograde with ecliptic longitudes near 210° and the other in the vicinity of the ecliptic equator with longitudes near 60° (see Fig. 8). For the purpose of making initial predictions for $B_{max}(\delta)$, we consider two more or less representative cases, a "prograde" model and a "retrograde" model, as specified in Table II. We consider the entire ensemble of shapes and pole directions in Section 5, where we combine our 1982 and 1991 radar data to place new constraints on Pallas' pole direction.

4 Vesta

Vesta's visual-wavelength lightcurves have been interpreted by several investigators to be caused primarily by albedo variations and, to a lesser extent, by variations in the

TABLE III
Pallas Dimensions and Pole Direction

(1) Ellipsoid Dimensions			(2) Pole Direction		
2a	2b	2c	λ	β	Reference
			228	+43	Schroll *et al.* (1976)
558 (8)	526 (12)	532 (30)			Wasserman *et al.* (1979)
			211	+38	Burchi and Milano (1983)
			44	+4	Zappalà and Kneževič (1984)
			200	+40	Binzel (1984)
			220	+15	*ibid.*
			49	+6	Burchi *et al.* (1985)
			227	+20	Lambert (1985)
559	528	499	54	−6	Magnusson (1986)
537 (29)	488 (11)	485 (11)	100	−22	Drummond and Hege (1988)
			295	+16	*ibid.*
583 (18)	527 (3)	409 (52)	71	−19	Drummond and Cocke (1989)
574 (10)	526 (3)	501 (2)			Dunham *et al.* (1990)*

(1) Dimensions of a triaxial ellipsoid approximation to Pallas' overall shape, as derived from various combinations of lightcurve, occultation, and speckle imaging data. Quoted uncertainties, when available, are in parentheses.
(2) Ecliptic longitude (λ) and latitude (β) of pole coordinates (B1950). The pole uncertainties are depicted in Fig. 8.
* Assumed Binzel's (1984) pole in their analysis.

asteroid's projected area (Magnusson 1986 and references therein). Albedo variations over Vesta's surface were observed at visual wavelengths in speckle images (Drummond *et al.* 1988) and recently in Hubble Space Telescope images (Zellner and Storrs 1995). Similar albedo markings are present at infrared wavelengths (Hainaut 1995). The detailed interpretation of the albedo variations and the related problem of determining the relative contributions of shape and albedo to the observed lightcurve have been the subject of some controversy (Cellino *et al.* 1987, Drummond *et al.* 1988, Tsvetkova *et al.* 1991). In particular, it remains unclear whether Vesta's shape is best described by an equilibrium figure (i.e., an oblate spheroid) or a nonequilibrium triaxial ellipsoid.

An independent estimate of Vesta's shape was provided by infrared speckle imaging (McCarthy *et al.* 1994). McCarthy *et al.* considered both triaxial ellipsoid and oblate spheroid solutions and concluded that either is acceptable, producing similar shapes and pole directions. Those authors reviewed all existing pole direction constraints for Vesta (including their own) and arrived at a "weighted-average" direction with ecliptic coordinates of $\lambda = 334°$ and $\beta = +56°$ and an uncertainty of 14°. Since the asteroid exhibits a weak but detectable double-peaked millimeter-wavelength lightcurve (Redman *et al.* 1992), we adopt the triaxial model and pole direction of McCarthy *et al.* as an a priori model for Vesta.

4. RADAR SCATTERING LAWS FOR ASTEROIDS

An asteroid radar model typically consists of a shape, which accounts for structures on scales from the target's overall dimensions down to the effective spatial resolution of the data, and an angular scattering law [$\sigma_0(\theta) = d\sigma/dA$, where dA is an element of surface area and θ is the angle of incidence], which quantifies effects of structure on smaller scales. A scattering law may be viewed as an empirical formula, chosen for its suitability to a particular data set or for its mathematical convenience. When specular reflection is the dominant backscatter mechanism, the scattering law contains information about surface (Fresnel) reflectivity and about roughness on scales much larger than the radar wavelength. Simpson and Tyler (1982) discuss the relationship between quasi-specular scattering laws and

TABLE IV
Three Quasi-specular Scattering Laws

Scattering Law	Parker Slope Probability Distribution: $p_P(\theta)$	Differential Radar Cross Section $\sigma_o(\theta) = d\sigma/dA$	Backscatter Gain for a Sphere: g
Cosine	$2(C+1)\cos^{2C+1}\theta$	$R(C+1)\cos^{2C}\theta$	$1 + \frac{1}{2}s_o^2 - \frac{1}{4}s_o^4 + \ldots$
Gaussian	$2C\sec^3\theta\,\exp(-C\tan^2\theta)$	$RC\sec^4\theta\,\exp(-C\tan^2\theta)$	$1 + \frac{1}{2}s_o^2 - \frac{1}{4}s_o^4 + \ldots$
Flat	$(C+1)\ u_s(\theta_{max} - \theta)$	$\frac{1}{2}R(C+1)\sec\theta\ u_s(\theta_{max} - \theta)$	$1 + \frac{1}{2}s_o^2 - \frac{1}{6}s_o^4 + \ldots$

(1) For all scattering laws listed, R is the Fresnel power reflection coefficient at normal incidence, and C is a roughness parameter, defined such that the adirectional rms slope is given by $S_0 = \tan(\theta_{rms}) = C^{-1/2}$. The backscatter gain ($g$) relates the measured OC radar albedo to the Fresnel reflectivity: $\hat{\sigma}_{OC} = gR$; the value given corresponds to a sphere with $\mu_C = 0$.

(2) These relationships hold only for the quasi-specular portion of a radar echo. We use a scattering law of the form $\rho\cos^n(\theta)$ to model echoes from Vesta, which contain a mixture of specular and diffuse power, but the parameters of the scattering law (ρ and n) do not necessarily have a direct physical relationship to the parameters R and C.

(3) The Flat scattering law assigns a uniform probability for slopes between zero and a cutoff angle (θ_{max}) given by $\sec(\theta_{max}) = 1 + C^{-1}$. The unit step function, $u_S(\phi)$, is zero for $\phi < 0$ and unity for $\phi > 0$. This scattering law is intended to approximate the measured slope distributions for some terrestrial surfaces (McCollom and Jakosky 1993).

statistical descriptions of surface slopes, providing a framework for relating any scattering law (even an empirical one) to a physical description of surface roughness and reflectivity.

Table IV gives expressions for the differential radar cross section and radar backscatter gain for three slope probability distributions we consider. Angular scattering laws of the form $\sigma_0(\theta) = \rho\cos^n\theta$ have been the most commonly used in asteroid radar astronomy (Jurgens and Goldstein 1976, Ostro *et al.* 1983, 1984, Hudson and Ostro 1994, Mitchell *et al.* 1995) and have a strong empirical basis. Shepard *et al.* (1995) show that quasi-specular scatter from a surface with self-affine (fractal) topography gives rise to a Gaussian angular scattering law with a scale-dependent rms slope. Radar estimates of rms slopes for the terrestrial planets and the Moon increase with decreasing wavelength (Pettengill 1978), suggesting that those surfaces may possess some self-affine characteristics (Shepard *et al.* 1995). Finally, the Flat law is intended to approximate measured slope distributions for some terrestrial surfaces (McCollom and Jakosky 1993), and is included to provide a markedly different slope distribution from the "bell-shaped" Cosine and Gaussian distributions.

Each scattering law is a two-parameter function of angle (θ) with respect to the mean surface normal. One parameter (R) is related to radar reflectivity, and a second parameter (C) is related to surface roughness. If specular reflection is the sole backscatter mechanism, then R is the Fresnel power reflection coefficient at normal incidence, and the adirectional rms slope ($s_0 = \tan\theta_{rms}$) is given by (Simpson and Tyler 1982)

$$s_0 = \langle\tan^2\theta\rangle^{1/2} = \left[\int_0^{\pi/2}\tan^2\theta\, p_P(\theta)\sin\theta\, d\theta\right]^{1/2} = C^{-1/2}, \quad (2)$$

where $p_P(\theta)$ is the slope probability distribution (Parker 1973). However, the nonzero SC cross sections of all three of our targets indicate that at least some of the OC echo power arises from some other mechanism(s), which need not produce equal amounts of OC and SC echo power for a given incident SC flux. We loosely term the collective echo from all such mechanisms the "diffuse" echo. By this definition, the SC echo is entirely diffuse.

Harmon and Ostro (1985) estimated the diffuse scattering parameters for Mars and summarized those for Mercury, Venus, and the Moon. Here, we define the diffuse polarization ratio (μ_C^D) as the ratio of SC to OC echo power for the diffuse component alone. The value of μ_C^D ranges from ~0.3 for Venus to ~0.5 for the Moon. The fraction of the total OC cross section that arises from diffuse mechanisms is given by the ratio μ_C/μ_C^D, where μ_C is the measured circular polarization ratio as defined in Section 2.

We do not know the value of μ_C^D for any of our targets, but if the polarization properties of the diffuse echoes from Ceres and Pallas are in the range estimated for the terrestrial planets and the Moon (Harmon and Ostro 1985 and references therein), then we expect that ~75–95% of the OC echo power arises from quasi-specular reflections from smooth surface elements; the higher percentage corresponds to a lunarlike surface. Therefore, we treat the

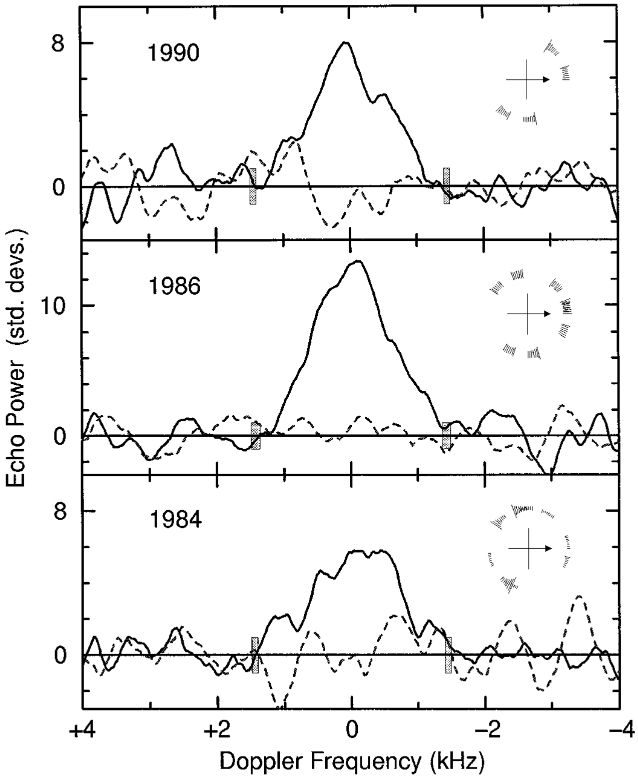

FIG. 1. Arecibo 13-cm radar spectra of 1 Ceres obtained in 1984, 1986, and 1990. Echo power, in standard deviations of the noise, is plotted versus Doppler frequency relative to that of hypothetical echoes from the asteroid's center of mass. The solid and dotted lines plot the OC and SC echoes, respectively, smoothed to a frequency resolution of 400 Hz. Each spectrum is a weighted sum of independent spectra obtained at different asteroid rotation phases, which are depicted in the inset with a radial "error bar" proportional to the standard deviation of each spectrum included in the average. The arrow indicates zero phase, which is arbitrarily assigned to the first spectrum obtained, and phase increases in the counterclockwise sense. There is no phase correspondence from year to year. The horizontal extent of the shaded boxes shows the expected range for the edge-to-edge bandwidth (B_{max}) based on external constraints on the asteroid's size, shape, and spin (see Table II).

OC echoes from Ceres and Pallas as if they were produced entirely by specular reflection. For Vesta, similar considerations suggest that less than half of the OC echo power arises from quasi-specular reflection. Thus, the strength and spectral distribution of OC echoes from Vesta could be strongly influenced (or even dominated) by diffuse scatter.

5. SURFACE PROPERTIES OF CERES, PALLAS, AND VESTA

In this section, we bring together the results from Sections 3 and 4 to model the echoes from each of our targets. Since each spectrum represents an average over many rotation phases, we replaced the triaxial ellipsoid shapes for Pallas and Vesta (Table II) with oblate spheroids and increased the uncertainty in each spheroid's equatorial diameter as we did for Ceres. Furthermore, we compared the spectrum produced by a sphere with that produced by an oblate spheroid for each target by holding the equatorial diameter fixed and decreasing the polar dimension within limits set by the a priori model. For our highest SNR data set (Pallas 1982), we found that for a given bandwidth (B), deviations from a spherical shape affect estimates of C by a negligible amount (smaller than the statistical uncertainty). The SNRs of all other data sets are insufficient to discriminate between a sphere and an oblate spheroid. Thus, at the risk of introducing only a slight bias, we can model each target as a sphere.

The Doppler spectrum of a sphere depends on (1) the limb-to-limb bandwidth, B, which is a function of the sphere's diameter and spin vector, and (2) the scattering law. We adopt uncertainties in the sphere's diameter and pole direction to provide a range for the model's bandwidth, B [via Eq. (1)], and search for the best-fit values of the scattering law parameters over this range.

1 Ceres

Figure 1 shows weighted sums of Arecibo echo spectra obtained in 1984, 1986, and 1990 smoothed to a resolution of 400 Hz, and Fig. 2 shows a weighted-sum spectrum from 1995 Goldstone 3.5-cm observations smoothed to 1500 Hz. As depicted in polar plots inset into the figures, each spectrum represents a weighted average of spectra from 4-min (Arecibo) or 2-min (Goldstone) integrations. In the polar plots, the standard deviation of the noise for each spectrum that contributes to the sum is represented by a radial "error bar" at the corresponding relative rotation phase. The first

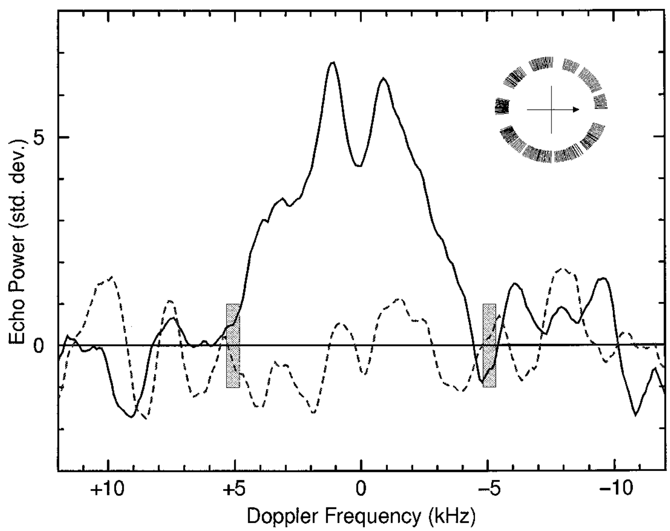

FIG. 2. Goldstone 3.5-cm radar spectrum of 1 Ceres obtained in 1995, smoothed to a frequency resolution of 1500 Hz. (See legend to Fig. 1.)

spectrum obtained for each apparition is arbitrarily assigned zero rotation phase, and there is no phase correspondence from year to year.

Table V shows estimates of Ceres' OC radar cross section, OC radar albedo, and circular polarization ratio from each of the four experiments. The radar cross section (σ_{OC}) is calculated from a weighted average of available spectra, and the radar albedo ($\hat{\sigma}_{OC}$) is estimated by dividing σ_{OC} by the projected area of the nominal a priori model averaged over all rotation phases. The quoted uncertainties (in parentheses) include all known sources of error, including the uncertainties in the axis dimensions and viewing geometry. The weighted average values of radar albedo and circular polarization ratio from all 13-cm radar observations of Ceres are $\langle\hat{\sigma}_{OC}\rangle = 0.042 \pm 0.006$ and $\langle\mu_C\rangle = 0.04 \pm 0.03$. Within the experimental uncertainties, our values for $\hat{\sigma}_{OC}$ and μ_C at 3.5 cm are consistent with corresponding values at 13 cm.

Ceres' low circular polarization ratios can be compared with lunar values at similar wavelengths as follows. Evans and Hagfors (1966) estimate that the total amount of echo power from the Moon associated with diffuse mechanisms is 25% at a wavelength of 23 cm and 35% at 3.6 cm. Based on dual-polarization measurements near the limb, where lunar echoes are almost entirely diffuse, μ_C^D is roughly 0.5 at both wavelengths (Evans and Hagfors 1966, Hagfors 1967, Zisk *et al.* 1974). Combining these results, we estimate disk-integrated values of μ_C for the Moon of ~0.09 at 23 cm and ~0.13 at 3.6 cm. Evidently, the surface of Ceres is smoother than the lunar surface at centimeter and deci-

TABLE V
Radar Properties by Experiment

(1) Target	Year	(2) OC SNR	(3) B_{EQ} (Hz)	(4) B_{HP}/B_{ZC}	(5) σ_{OC} (km^2)	(6) μ_C	(7) $\hat{\sigma}_{OC}$
Ceres (A)	1984	10	900	—	32400 (8400)	0.04 (0.06)	0.047 (0.012)
	1986	21	1510	0.51	24700 (6300)	0.04 (0.04)	0.036 (0.009)
	1990	11	980	—	31700 (8100)	0.02 (0.06)	0.046 (0.012)
Ceres (G)	1995	11	4140	—	25600 (6600)	0.00 (0.07)	0.037 (0.010)
Pallas (A)	1982	52	590	0.55	19000 (4800)	0.05 (0.02)	0.081 (0.021) †
							0.096 (0.025) ‡
	1987	8	300	—	19600 (4900)	—	0.084 (0.021) †
							0.084 (0.021) ‡
	1991	19	1060	0.51	14500 (3700)	0.05 (0.05)	0.066 (0.017) †
							0.081 (0.023) ‡
Vesta (A)	1981	11	890	—	11700 (3000)	—	0.058 (0.015)
	1988	11	1020	—	22600 (5900)	0.24 (0.06)	0.112 (0.030)
	1992	13	1430	0.49	17200 (4400)	0.24 (0.05)	0.086 (0.023)
Vesta (G)	1992	22	7150	0.51	30200 (7700)	0.32 (0.04)	0.150 (0.040)

(1) Observed target with radar system in parentheses: A = Arecibo (13-cm wavelength), G = Goldstone (3.5-cm wavelength).

(2) Signal-to-noise ratio for an optimally filtered, weighted sum of all OC spectra from an experiment.

(3) By definition (Tiuri 1964), $B_{EQ} = \Delta f[(\Sigma S_i)^2/\Sigma S_i^2]$, where S_i are the spectral elements, and Δf is the "raw" frequency resolution.

(4) B_{HP} and B_{ZC} are the half-power and zero-crossing bandwidths, respectively, of the weighted sum of all OC spectra from an experiment smoothed to a frequency resolution of $B_{EQ}/10$. No ratio is listed if the half-power level is less than three standard deviations above the noise.

(5) σ_{OC} is the OC radar cross section. Assigned uncertainties are the root sum square of systematic calibration errors, estimated as 25% of the cross-section values, and the standard deviation of the receiver noise in the equivalent bandwidth (B_{EQ}).

(6) μ_C is the circular polarization ratio (of SC to OC echo power). The standard deviations quoted for μ_C propagate from the receiver noise alone. Calibration difficulties for the SC channel of the 1987 Pallas and the 1981 Vesta spectra do not permit reliable estimates for μ_C on those dates.

(7) The radar albedo, $\hat{\sigma}_{OC}$, is obtained by dividing σ_{OC} by the average projected area of the a priori model ellipsoid at the epoch of our observations. Uncertainties propagate from those given for σ_{OC} and $\langle A_P\rangle$. For Pallas the first radar albedo estimate (†) is based on the "prograde" model (shape given by Dunham *et al.* 1990, with Binzel's 1984 pole), and the second estimate (‡) is based on the "retrograde" model (shape and pole given by Drummond and Cocke 1989).

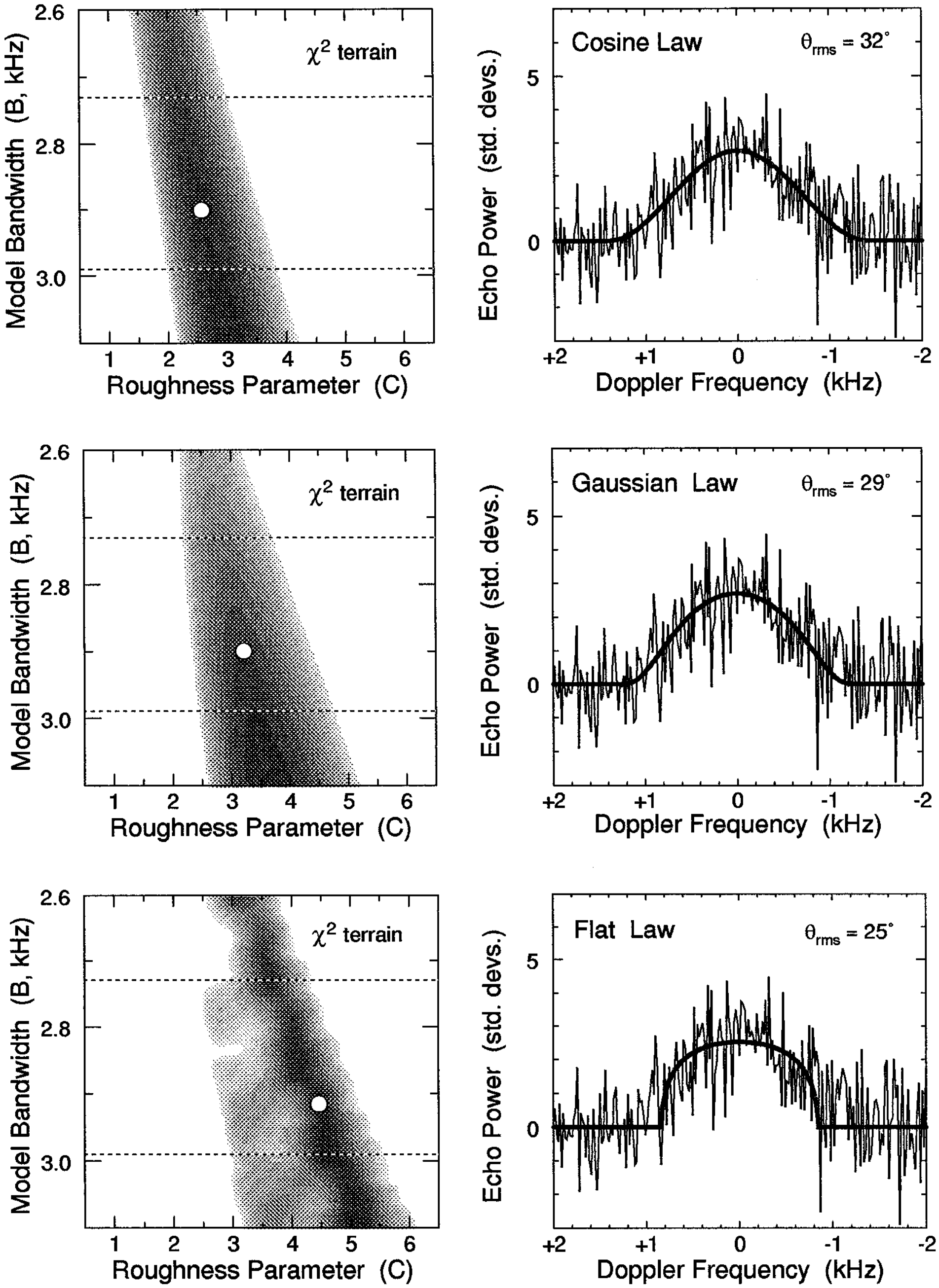

FIG. 3. Least-squares fits to a 13-cm-wavelength radar spectrum of 1 Ceres obtained at Arecibo in 1986, shown at the raw frequency resolution of 18.8 Hz. The model, a rough-surface sphere, is specified by a bandwidth, B, which depends on the sphere's size and spin vector, and a roughness parameter, C, which for this low-μ_C target is related to the rms surface slope ($\tan \theta_{rms} = C^{-1/2}$). The results for three different assumed scattering laws are shown (see Table IV). The parameters B and C are highly correlated, as shown by the elongated χ^2 troughs on the left. (The shaded area corresponds roughly to the 1-σ uncertainty region. The structure in χ^2 (B, C) for the Flat law model arises from its very sharp spectral edges in combination with the high noise level, and does not have physical significance.) Independent information is essential to resolve this B–C ambiguity. The bandwidth is expected to be within the range 2.73–2.99 kHz (dashed lines) based on lightcurve, occultation, and speckle data. This allows us to constrain the roughness parameter, C (see Table VI). The parameters of the model spectrum on the right correspond to the coordinates of the white circle on the left.

meter scales, presumably because of differences in material strength (see Section 6).

The horizontal extents of the shaded boxes in Figs. 1 and 2 encompass interval estimates for hypothetical echoes from Ceres' limbs based on B_{max} (δ) for the nominal shape and pole direction (Table II) and the uncertainties therein. Note that all of the gray boxes have the same maximum extent in frequency, which is a firm upper limit correspond-

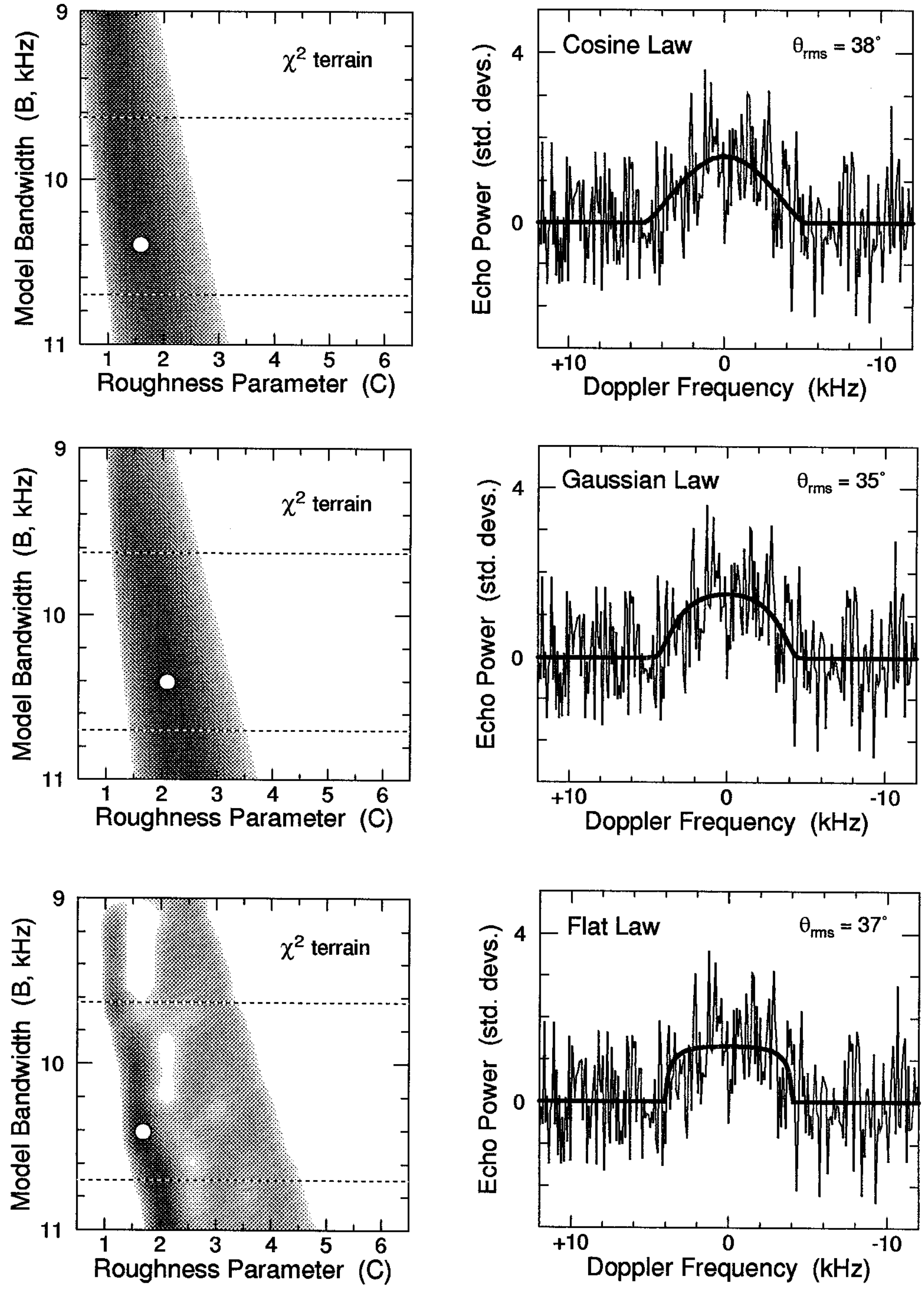

FIG. 4. Least-squares fits to a 3.5-cm-wavelength radar spectrum of 1 Ceres obtained at Goldstone in 1995, shown at the raw frequency resolution of 97.7 Hz. (See legend to Fig. 3.) The bandwidth is expected to be within the range 9.63–10.66 kHz (dashed lines).

ing to an equatorial view of Ceres with the maximum 980-km equatorial diameter. The apparent extents of the OC spectra (i.e., the bandwidths between first zero crossings) are nearly as wide as the a priori bandwidth constraints, which indicates that echo power is observed close to the limbs.

Figure 3 shows least-squares estimations of the parameters B and C for three different scattering laws (Table IV) based on fits to the 1986 OC spectrum. Figure 4 shows least-squares results for the 1995 Goldstone spectrum. A grayscale representation of the function $\chi^2(B, C)$ is shown in the left panel for each scattering law. The parameters B and C are highly correlated, as shown by the elongated χ^2 trough, which extends well beyond the plot boundaries. However, the limb-to-limb bandwidth of the a priori model falls between the dashed lines, which allows us to constrain the roughness parameter, C.

The Cosine and Gaussian scattering laws provide slightly better fits to the observed spectral shape, but the Flat law cannot be ruled out. There are, no doubt, other scattering laws that would provide equally good fits. However, there is considerable overlap in the χ^2 troughs for all three of our scattering laws, which suggests that the least-squares estimate of C for a given value of B is not particularly sensitive to the form of the slope probability distribution. Thus, our inferences about rms slope rest primarily on the frequency distribution of the echo power relative to nonradar constraints on B.

The a priori bandwidths correspond to nearly equatorial views, so B, and hence C, cannot be made any larger because of uncertainty in the pole direction. Our constraints on C (Table VI) correspond to rms slopes of 20°–40° at the 13-cm wavelength and 25°–50° at the 3.5-cm wavelength. A similar trend of increasing rms slope with decreasing radar wavelength is observed for the lunar maria, where rms slope estimates are typically 5° at a wavelength of 13 cm and half as large at 116 cm (Simpson and Tyler 1982). This behavior is believed to be related to differences in surface roughness on scales near the wavelength (Tyler 1979), possibly resulting from self-affine topography (Shepard *et al.* 1995), at least over the range of length scales applicable here. The presence of wavelength-scale roughness is consistent with a nonzero circular polarization ratio and serves as a reminder of the limitations of our radar model.

2 Pallas

Figure 5 shows weighted sums of Arecibo echo spectra obtained in 1982, 1987, and 1991. Estimates of radar cross section and circular polarization ratio are given for all three apparitions in Table V. Like Ceres, Pallas has a very low 13-cm-wavelength circular polarization ratio ($\mu_C \approx 0.05$), indicating that most of the echo power originates from specular reflections from surface elements that are smooth from centimeter to meter scales. Radar albedo estimates based on the prograde and retrograde models differ in part because of the retrograde model's shorter polar dimension, but regardless of which model is assumed, Pallas' OC radar albedo is significantly higher than that of Ceres.

Predicted ranges for $B_{max}(\delta)$ based on the prograde and retrograde models are shown by shaded boxes for

TABLE VI
Spherical Model Results

(1)	(2)	(3)			(4)		
		Arecibo 13-cm			Goldstone 3.5-cm		
Target	Scattering Law	B (Hz)	C	χ^2_ν	B (kHz)	C	χ^2_ν
1 Ceres	Cosine	2730 – 2990	2.6 ± 1.2	1.10	9.6 – 10.7	1.7 ± 1.1	1.08
	Gaussian	2730 – 2990	3.3 ± 1.3	1.11	9.6 – 10.7	2.2 ± 1.1	1.08
	Flat	2730 – 2990	4.5 ± 2.5	1.14	9.6 – 10.7	2.7 ± 1.7	1.09
2 Pallas	Cosine	850 ± 33	2.0 ± 0.3	1.10			
(1982)	Gaussian	1110 ± 75	4.6 ± 0.8	1.10		no data	
	Flat	416 – 2130	poor fit	> 1.22			
	Cosine	1620 – 2130	2.8 ± 1.8	0.98			
(1991)	Gaussian	1620 – 2130	3.5 ± 1.9	0.98		no data	
	Flat	1620 – 2130	4.6 ± 3.0	1.00			
		B (Hz)	n	χ^2_ν	B (kHz)	n	χ^2_ν
4 Vesta	$\rho\cos^n(\theta)$	2170 – 3010	2.2 ± 1.2	1.12	7.8 – 10.7	2.0 ± 1.0	1.10

(1) The radar spectra used to constrain the models are as follows: Ceres (Arecibo 1986, Goldstone 1995), Pallas (Arecibo 1982, Arecibo 1991), and Vesta (Arecibo 1992, Goldstone 1992). See Table I for details of observations.

(2) For Ceres and Pallas, the model is a sphere with one of three different radar scattering laws: Cosine, Gaussian, or Flat (see Table IV). For Vesta, the model is a sphere with a $\rho \cos^n(\theta)$ scattering law. Each model is specified by a bandwidth (B), which depends on the sphere's size and spin vector, and a roughness parameter (C or n).

(3) Model parameters at 13-cm wavelength. Except for the Cosine and Gaussian fits to the 1982 Pallas data, the specified ranges for B are based on external constraints (see Table II), except that the upper bound is increased to correspond with an equatorial view. Parameter uncertainties are one standard deviation and account for the correlation between B and C (or between B and n) over the range specified for B. See Figs. 3, 4, 6, 7, and 11 for details of parameter estimation.

(4) Model parameters at 3.5-cm wavelength.

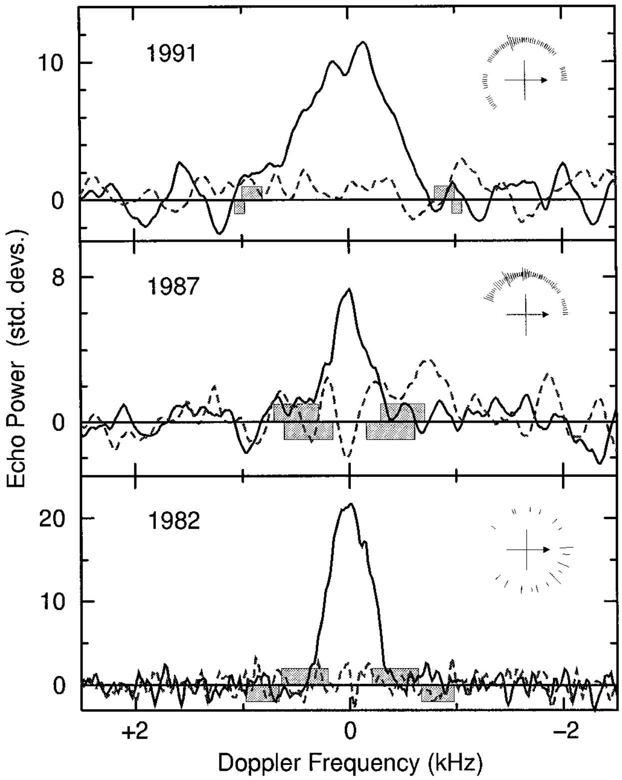

FIG. 5. Arecibo radar spectra of 2 Pallas obtained in 1982, 1987, and 1991. The solid and dotted lines plot the OC and SC echoes, respectively, smoothed to a frequency resolution of 60 Hz (1982 spectrum) or 200 Hz (1987 and 1991 spectra). The notation is the same as in Fig. 1. The upper gray box corresponds to bandwidth constraints derived from the "prograde" model of Dunham *et al.* (1990); the lower gray box corresponds to bandwidth constraints derived from the "retrograde" model—see Table II.

comparison with the apparent spectral edges (the innermost zero crossings) for each year. The two models provide distinct bandwidth predictions for the 1982 apparition. The prograde model predicts a narrower bandwidth (upper shaded boxes), which would indicate that echo power is detected from regions close to the asteroid's limbs (as is the case for Ceres). The retrograde model predicts a wider bandwidth (lower shaded boxes), which would indicate that echo power is detected from regions that are more confined to the subradar point—analogous to but still much broader than the "specular spike" in OC echoes from the Moon and Mercury (e.g., Butler *et al.* 1993). However, both models provide similar bandwidth predictions for the 1987 and 1991 radar apparitions, which suggests that our radar data may provide additional leverage on Pallas' shape and pole direction.

Figure 6 shows least-squares estimations of the parameters B and C based on fits to the 1982 OC spectrum. This is our highest SNR spectrum, so the formal B–C uncertainty region is significantly smaller than for our other data sets. Again, we see significant overlap in the χ^2 troughs for all three scattering laws; however, the Flat law yields poor fits for all values of B (see Table VI), so we confine our attention to the Cosine and Gaussian laws. Global χ^2 minima exist for the Cosine and Gaussian laws, and both would favor the prograde model (see also OCS85); however, we do not know the "true" scattering law, so we cannot attach physical significance to either global minimum. Furthermore, since B and C can be anywhere within the shaded χ^2 trough, we cannot rule out the retrograde model based on the 1982 spectrum alone.

Figure 7 shows least-squares results in the 1991 OC spectrum. Both the prograde and retrograde models predict a more equatorial view during the 1991 apparition, which is consistent with the wider apparent bandwidth in that year (Fig. 5). Again, the parameters B and C are constrained within a χ^2 trough, but there are no global minima. Since our view is nearly equatorial, the a priori information on Pallas' dimensions (Table III) places a useful upper bound on B without regard to the pole direction: $B_{1991} \leq 2130$ Hz (lower dashed line in Fig. 7). This bound results in $C \leq 4.6$ for the Cosine law and $C \leq 5.4$ for the Gaussian law, which represent lower bounds on the roughness of Pallas' surface. (We ignore the Flat law results for the 1991 spectrum based on that law's poor fit to the 1982 spectrum.)

The combined least-squares results for the 1982 and 1991 Pallas spectra allow us to place more stringent constraints on its pole direction. Previous radar constraints on Pallas' pole (Ostro 1987) were necessarily conservative because they were based on only a single apparition. Basically, radar observations from a single apparition place a firm lower bound on the limb-to-limb bandwidth (there must be surface area where one detects echo power), but the upper bound is quite "soft" since there may be no way of knowing how close the apparent spectral edges are to the Doppler frequencies of the target's limbs. We can "firm up" the upper bound on B_{1982} since the 1991 spectrum establishes a minimum surface roughness for Pallas. Applying the upper bounds on C from the 1991 apparition to the Cosine and Gaussian law fits of the 1982 spectrum (Fig. 6), we find $B_{1982} \leq 1300$ Hz, which is independent of the pole direction.

We obtain lower bounds to B_{1982} and B_{1991} by noting that all of the least-squares fits yield minimum bandwidths independent of nonradar constraints: $B_{1982} \geq 650$ Hz and $B_{1991} \geq 1350$ Hz. We did not attempt to fit the low-SNR 1987 spectrum, but B_{EQ} (Table V) serves as a conservative lower bound to the bandwidth (Ostro 1987), which yields $B_{1987} \geq 300$ Hz.

All of the above bandwidth constraints can be converted into constraints on $\cos(\delta)$ via Eq. (1) if we assume that $2b \leq D(\phi) \leq 2a$, where the axial dimensions a and b are those of either the prograde or the retrograde model. For each apparition, the constraint on $\cos(\delta)$ defines two annuli on the celestial sphere (corresponding to $\pm\delta$) where the asteroid's pole may be found: one centered on the asteroid's coordinates during the radar observa-

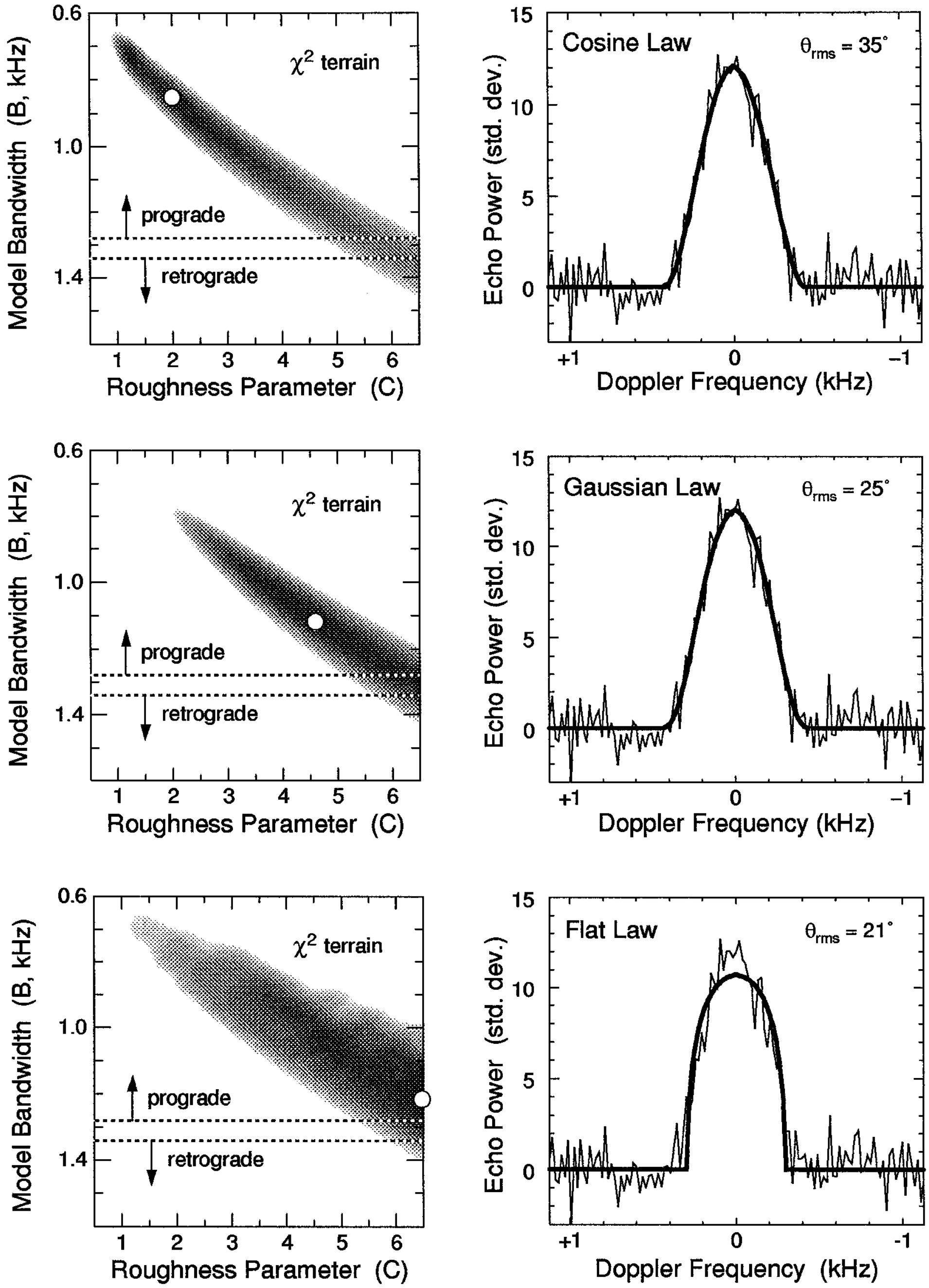

FIG. 6. Least-squares fit to a 13-cm-wavelength radar spectrum of 2 Pallas obtained at Arecibo in 1982, shown at the raw frequency resolution of 18.8 Hz. (See legend to Fig. 3.) The dashed lines show an *upper limit* to the bandwidth based on the "prograde" model and a *lower limit* based on the "retrograde" model (Table II). Note that global χ^2 minima exist for the Cosine and Gaussian law models (white circles on the left), but the locations of the minima are model dependent and do not necessarily have physical significance. The Flat law model produces poor fits for all bandwidths up to 2.07 kHz, corresponding to an equatorial view.

tion, and a second that is a mirror projection of the first (Mitchell *et al.* 1995). The regions for the pole coordinates that are consistent with all three apparitions are defined by the intersections of all annuli, as illustrated in Fig. 8. There is considerable overlap between our radar pole constraints and the nonradar pole directions with ecliptic longitudes near 210° (directions 1, 2, 4, 5, and 7).[2] The agreement is generally not as good as nonradar pole directions with ecliptic longitudes near 60° (directions 3, 6, 8, and 11), and directions 9 and 10 are clearly incompatible with the radar constraints.

[2] For ease of reference, we identify each nonradar pole direction by a number from 1 to 11, as defined in Fig. 8.

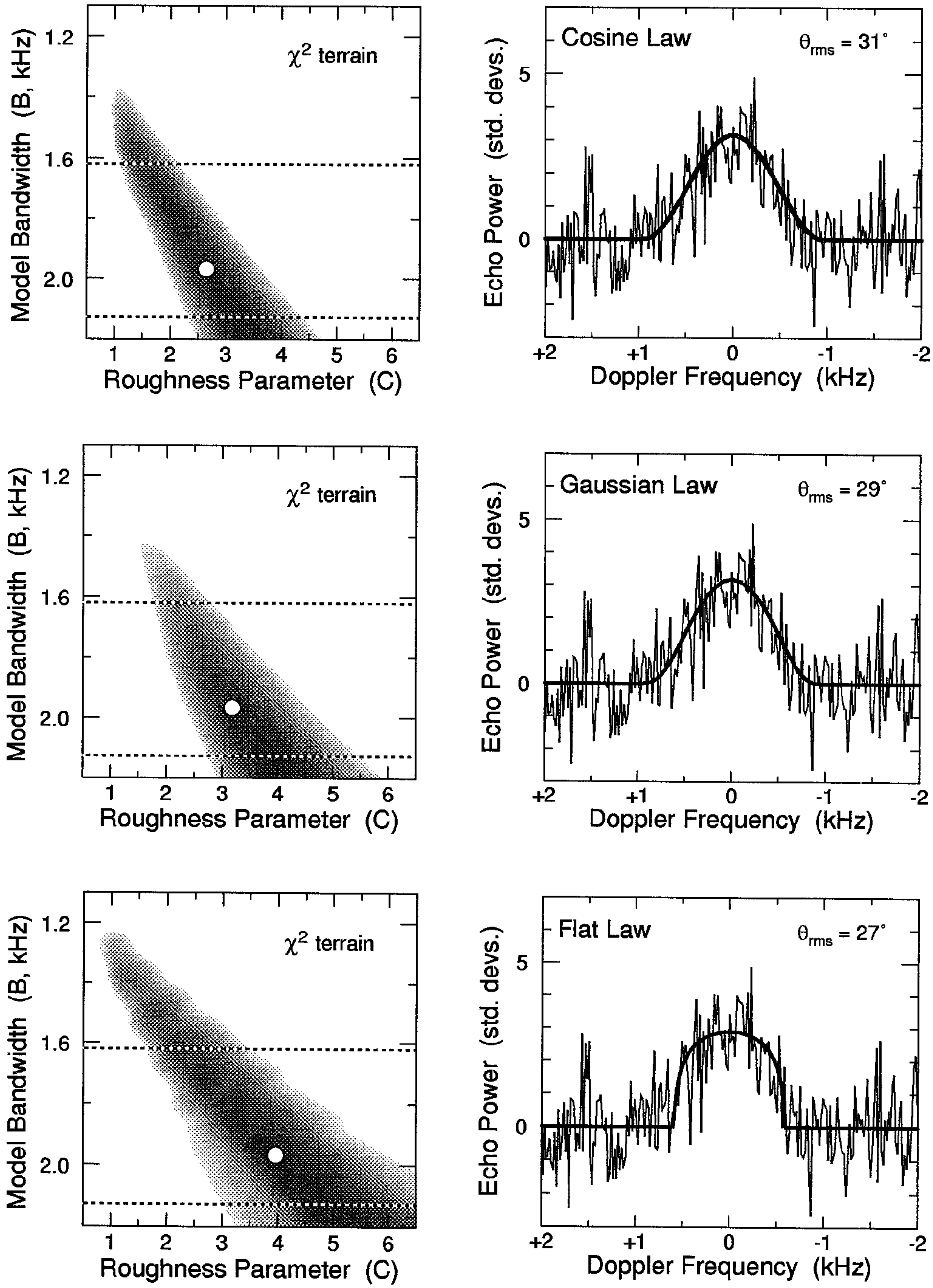

FIG. 7. Least-squares fits to a 13-cm-wavelength radar spectrum of 2 Pallas obtained at Arecibo in 1991, shown at the raw frequency resolution of 18.8 Hz. (See legend to Fig. 3.) The bandwidth is expected to be within the range 1.62–2.13 kHz (dashed lines), with the upper limit corresponding to an equatorial view.

The prograde model's pole direction (5) is favored over that of the retrograde model (11), so we adopt the prograde model's shape and pole direction for the purpose of estimating radar scattering properties. The interval estimate for the roughness parameter based on the prograde model (which predicts $B_{1991} \leq 1990$ Hz) and the combined 1982 and 1991 least-squares results is $1.0 \leq C \leq 4.7$, which corresponds to $25° \leq \theta_{\rm rms} \leq 45°$. This is very similar to the result for Ceres, and both asteroids also have nearly the same circular polarization ratio. Evidently, surface roughness at decimeter scales and larger is very similar on Ceres and Pallas. However, our estimate for Pallas' radar albedo (Table VII) is nearly twice that of Ceres, which indicates a significant difference in surface bulk density. We return to this issue in Section 6.

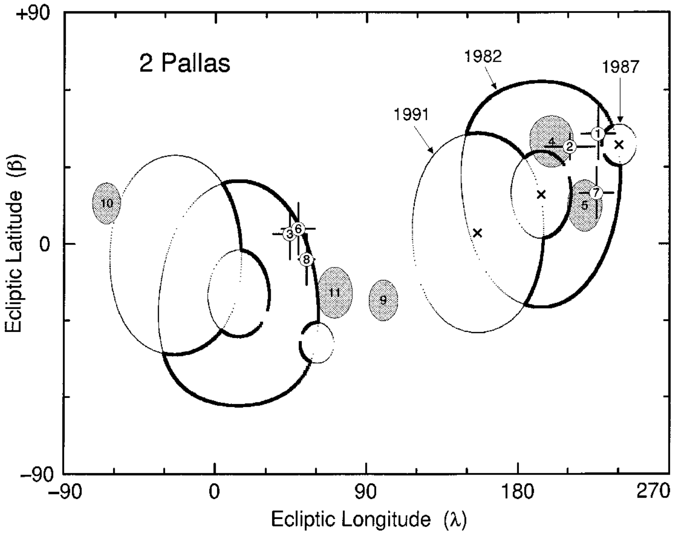

FIG. 8. Comparison of radar constraints on Pallas' pole direction with other published pole directions shown in a rectangular projection of geocentric ecliptic coordinates. The target's position during each radar apparition is shown by an "x", and the pole constraints for each apparition taken separately are shown by the dotted annuli, one centered on the coordinates of the asteroid at the time of the radar observation and another that is a mirror projection of the first. The annuli for 1987 and 1991 are so broad that they merge and fill up the entire region outside of their inner edges. The intersections of the annuli (outlined in bold) define two possible regions for the pole coordinates that are consistent with all spectra. The nonradar pole directions and their quoted uncertainties are shown as points with error bars or as shaded regions, which are numbered as follows: (1) Schroll *et al.* (1976); (2) Burchi and Milano (1983); (3) Zappalà and Knežević (1984); (4,5) Binzel (1984); (6) Burchi *et al.* (1985); (7) Lambert (1985); (8) Magnusson (1986); (9,10) Drummond and Hege (1989); (11) Drummond and Cocke (1989).

4 Vesta

Figure 9 shows weighted sums of Arecibo echo spectra obtained in 1981, 1988, and 1992, and Fig. 10 shows a weighted-average spectrum obtained at Goldstone in 1992. Estimates of radar cross section and circular polarization ratio for all apparitions are given in Table V. Estimates of Vesta's radar albedo based on the a priori ellipsoid model exhibit a larger variation from year to year than do radar albedo estimates for either Ceres or Pallas. These might be partly related to hardware upgrades to the Arecibo radar system made after 1981 observations but prior to any of the other observations discussed here. Alternatively, possible radar reflectivity variations across Vesta's surface might be sampled differently in each year, thus biasing the radar albedo estimates; however, our echoes do not have sufficient SNR to test this hypothesis. Based on these considerations, we prefer to report the *un*weighted average and standard deviation of the Arecibo radar albedo estimates: $\langle \hat{\sigma}_{OC} \rangle = 0.085 \pm 0.027$ (Table VII). Vesta has a high circular polarization ratio, which increases from $\mu_C = 0.24 \pm 0.04$ at the 13-cm wavelength to $\mu_C = 0.32 \pm 0.04$ at 3.5 cm. By this measure, Vesta's surface is rougher than the lunar surface at decimeter and centimeter scales.

Predicted ranges for $B_{max}(\delta)$ based on the a priori ellipsoid and pole direction are shown by shaded boxes for comparison with the apparent spectral edges for each year. The maximum frequency extents of the boxes are nearly the same from year to year, and all correspond to a subradar latitude within 10° of Vesta's equator. As was the case for Ceres, the apparent extents of the OC spectra are nearly as wide as the a priori bandwidth constraints. However, Vesta's circular polarization ratio is much higher than that of Ceres, indicating that backscatter mechanisms other than specular reflection could significantly affect the echo's strength and spectral distribution.

Figure 11 shows least-squares results for the Arecibo and Goldstone OC spectra obtained in 1992. Since scattering from wavelength-scale structures could dominate the echoes, we cannot safely make inferences about Fresnel reflectivity or surface slopes on scales much larger than the wavelength. In other words, the physical relationships outlined in Table IV probably do not apply to Vesta. To

TABLE VII
Average Radar Properties

		Arecibo 13-cm		Goldstone 3.5-cm	
Target	Class	$\langle \mu_C \rangle$	$\langle \hat{\sigma}_{OC} \rangle$	μ_C	$\hat{\sigma}_{OC}$
Ceres	G	0.04 (0.03)	0.042 (0.006)	0.00 (0.07)	0.037 (0.010)
Pallas	B	0.05 (0.02)	0.075 (0.011)	—	—
Vesta	V	0.24 (0.04)	0.084 (0.027)	0.32 (0.04)	0.150 (0.040)

Note. Weighted averages of μ_C and $\hat{\sigma}_{OC}$ from all Arecibo radar experiments for each target, except for Vesta, where $\langle \hat{\sigma}_{OC} \rangle$ represents an unweighted average (see text). For Pallas, we have adopted the "prograde" model (shape given by Dunham *et al.* 1990, with Binzel's 1984 pole) based on new pole constraints provided by the combined 1982 and 1991 radar spectra (see text). Values at 3.5 cm for Ceres and Vesta are from single apparitions.

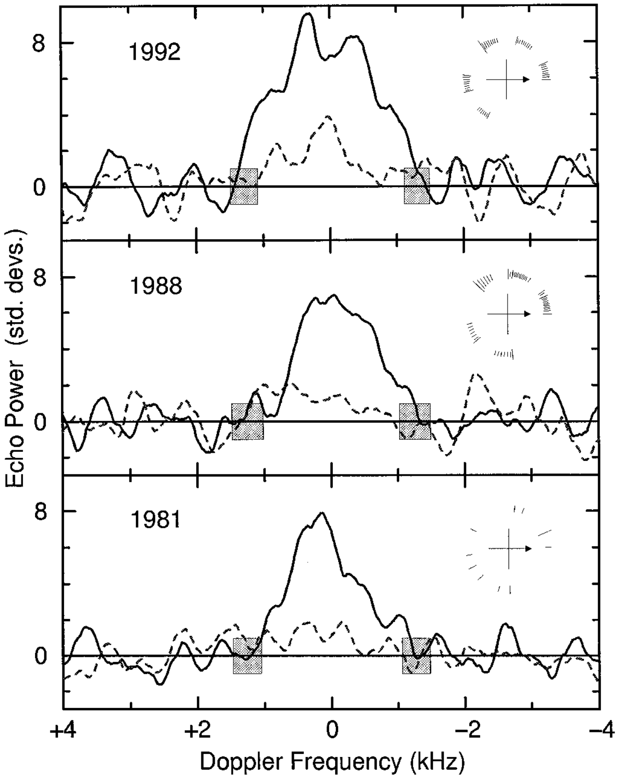

FIG. 9. Arecibo radar spectra of Vesta obtained in 1981, 1988, and 1992. The solid and dotted lines plot the OC and SC echoes, respectively, smoothed to a frequency resolution of 400 Hz. The notation is the same as in Fig. 1.

emphasize this fact, we present least-squares results for Vesta only in terms of a $\rho \cos^n(\theta)$ scattering law, which is mathematically equivalent to the Cosine law in Table IV. Vesta's 13-cm scattering law exponent, $n = 2.2 \pm 1.2$, is similar to those obtained for the ECAs 4769 Castalia ($n = 2.8 \pm 0.3$; Hudson and Ostro 1994), which has $\mu_C \approx 0.3$ (Ostro *et al.* 1990), and 4179 Toutatis ($n = 2.3 \pm 0.5$; Hudson and Ostro 1995), which has circular polarization ratios between 0.2 and 0.4 at wavelengths from 3.5 to 13 cm (S. J. Ostro, unpublished data). Empirically, scattering laws of the form $\rho \cos^n(\theta)$ seem to work equally well for specular and diffuse scattering from asteroids.

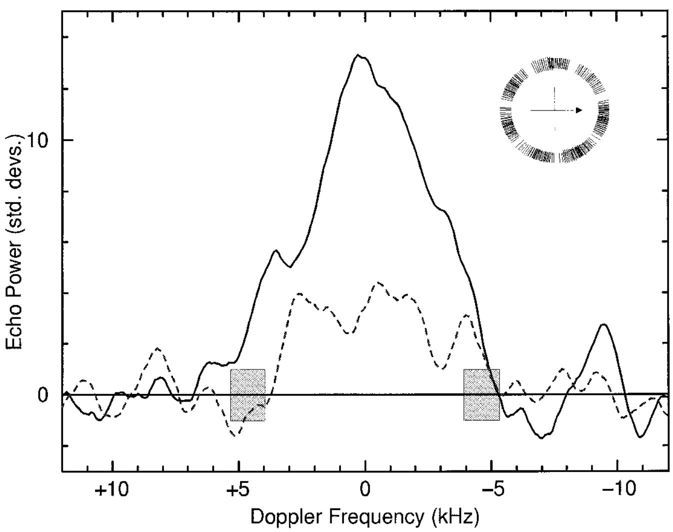

FIG. 10. Goldstone 3.5-cm radar spectrum of Vesta obtained in 1992, smoothed to a frequency resolution of 900 Hz. (See legend to Fig. 1.)

6. IMPLICATIONS OF THE RADAR MODELS

Radar Albedos: Ceres versus Pallas

Table VII lists values of μ_C and $\hat{\sigma}_{OC}$ for each of our targets based on all Arecibo and Goldstone observations since 1981. As noted above, the low circular polarization ratios for Ceres and Pallas indicate that specular reflection is the dominant backscatter mechanism, so that $\hat{\sigma}_{OC} = gR$, where g is the radar backscatter gain (OCS85), may be used to constrain the normal reflectivity R. The 13-cm-wavelength roughness parameter constraints for Ceres ($1.4 \leq C \leq 7.0$) and Pallas ($1.0 \leq C \leq 4.7$) provide very similar estimates of the backscatter gain for both targets (see Table IV). Therefore, the difference in radar albedos cannot be attributed entirely to g but rather implies that the normal reflectivity of Pallas' surface is higher than that of Ceres. If we adopt $g = 1.15 \pm 0.10$ for both targets, then the 13-cm-wavelength radar albedos given in Table VII correspond to normal reflectivities of $R = 0.037 \pm 0.006$ for Ceres and $R = 0.065 \pm 0.011$ for Pallas.

As discussed by OCS85 and Ostro *et al.* (1991), R depends almost linearly on bulk density (d) for mixtures of dry, particulate meteoritic minerals. An empirical relation (Garvin *et al.* 1985) applicable for porosities greater than ~20% is

$$d(R) = 3.2 \ln \left[\frac{1 + \sqrt{R}}{1 - \sqrt{R}}\right]. \tag{3}$$

With this relation, the above reflectivities correspond to $d = 1.24 \pm 0.10$ g cm^{-3} for Ceres and $d = 1.66 \pm 0.15$ g cm^{-3} for Pallas, each of which provides a joint constraint on the regolith porosity and the specific gravity (zero-porosity density; see Carrier *et al.* 1991) of the surface material, as illustrated in Fig. 12.

The difference in bulk densities could be related to porosity. For example, if the surface materials on both asteroids have a specific gravity of 2.6 g cm^{-3}, then Ceres and Pallas would have regolith porosities of 50 and 35%, respectively, which are in the range of lunar regolith porosities (Carrier *et al.* 1991). While we cannot exclude this possibility, we know of no other evidence that would support such a conclusion, as the surfaces of both asteroids have similar thermal inertias (Spencer *et al.* 1989) and optical polarization properties (Dollfus *et al.* 1989).

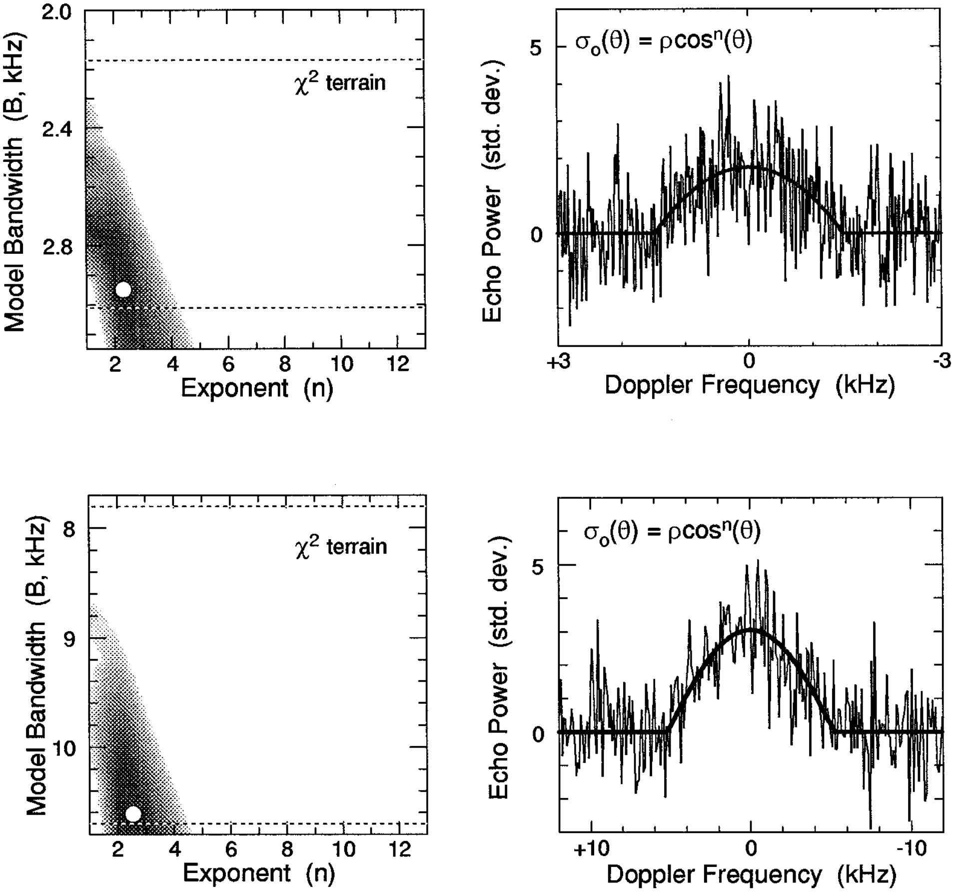

FIG. 11. (*Upper*) Least-squares fit to a 13-cm-wavelength radar spectrum of 4 Vesta obtained at Arecibo in 1992, shown at the raw frequency resolution of 18.8 Hz. (See legend to Fig. 3.) Vesta's high circular polarization ratio ($\mu_C = 0.24 \pm 0.04$) indicates a significant contribution from nonspecular scattering mechanisms, so we use an empirical $\rho \cos^n(\theta)$ scattering law instead of the quasi-specular laws of Table IV (see text). The bandwidth is expected to be within the range 2.17–3.01 kHz (dashed lines). The upper limit corresponds to an equatorial view. (*Lower*) Least-squares fit to a 3.5-cm-wavelength radar spectrum of 4 Vesta obtained at Goldstone in 1992, shown at the raw frequency resolution of 97.7 Hz. The bandwidth is expected to be within the range 7.8–10.7 kHz (dashed lines). The upper limit corresponds to an equatorial view.

Alternatively, Ceres and Pallas could have the same regolith porosity but distinct surface mineralogies. Given a porosity of 45%, the surface materials on Ceres and Pallas would have specific gravities of 2.3 and 3.0 g cm^{-3}, respectively, which are in the range for carbonaceous chondrite meteorites (Fig. 12). Detailed analyses of visual/infrared reflectance spectra of Ceres and Pallas (Feierberg *et al.* 1981, Lebofsky *et al.* 1981, Larson *et al.* 1983) suggest surface mineralogies consisting of aqueously altered carbonaceous chondrite matrix material (CCMM, such as that found in CI and CM meteorites), with an additional Fe^{2+}-poor anhydrous silicate component (e.g., CM chondrules) for Pallas. For a given porosity, adding such a silicate component to CCMM would increase the bulk density and hence the radar reflectivity of the surface. Thus, Pallas' higher radar albedo could be a manifestation of mineralogical differences between Ceres and Pallas.

Further support for this last hypothesis can be found in recent mass estimates for Ceres and Pallas based on their perturbations to the orbit of Mars and on close encounters with other asteroids (M. Carpino, personal communication, see also http://www.mi.astro.it/~carpino). If we adopt masses for Ceres and Pallas based on the JPL DE403 ephemeris (Standish *et al.* 1995, E. M. Standish, personal communication), $M_{\mathrm{Ceres}} = 4.64 \pm 0.2$ and $M_{\mathrm{Pallas}} = 1.05 \pm 0.2$ (units of 10^{-10} M_{Sun}), and divide each by the volume of the corresponding a priori ellipsoid (Table II), then we obtain mean densities of $\langle\rho\rangle_{\mathrm{Ceres}} = 2.1 \pm 0.1$ and $\langle\rho\rangle_{\mathrm{Pallas}} = 2.6 \pm 0.5$ g cm^{-3}. As before, any difference in mean density can be attributed to either porosity or specific gravity. We show the mean density estimates in Fig. 12 for the case of negligible volume-averaged porosity. (Both estimates would move upward on the plot to the extent that this assumption is invalid.) Although the estimates overlap, there is some indication that the mean density of Pallas is higher than that of Ceres, which would be consistent with the mineralogical differences discussed above.

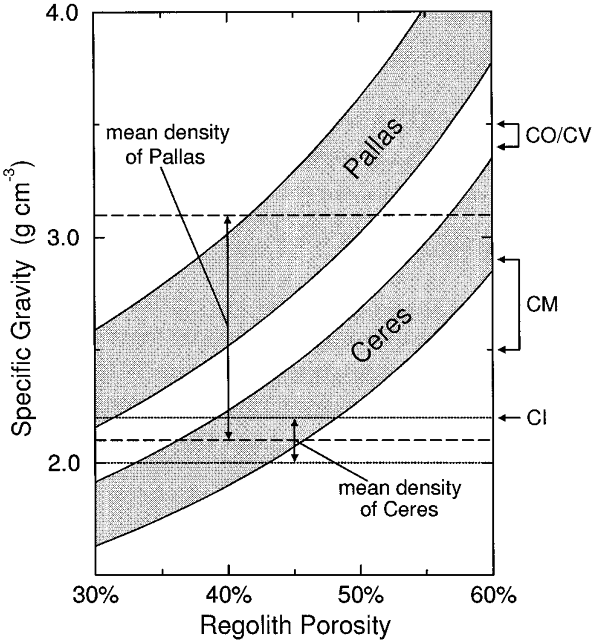

FIG. 12. Radar constraints on the surface densities of Ceres and Pallas provide a joint constraint on regolith porosity and specific gravity (zero-porosity density) (shaded regions). These are compared with typical densities of solid carbonaceous chondrite meteorites (types CI, CM, CO, and CV from Table 4.6 of Glass 1982). Constraints on the *mean* densities of Ceres (dotted lines) and Pallas (dashed lines) are obtained by dividing each object's total mass by the volume of its a priori shape (see text).

Decimeter-Scale Surface Roughness: Ceres and Pallas versus Vesta

All three of our targets possess very rough surfaces. For Ceres and Pallas, the combination of low polarization ratios and large rms slopes indicates that their surfaces are quite smooth on centimeter-to-meter scales but very rough on larger scales. In contrast, Vesta's high circular polarization ratio reveals abundant decimeter-scale roughness. Ceres, Pallas, and Vesta are thought to be covered by at least tens of meters of regolith, which is generated and modified by impacts (McKay *et al.* 1989 and references therein). The amount, size distribution, and placement of retained impact ejecta depend on the target's size and strength (Cintala *et al.* 1978, Housen *et al.* 1979), while the evolution of the regolith's particle size distribution, and in particular the abundance of decimeter-sized rocks, depends on the asteroid's impact history and on the strength of the regolith material.

Pallas and Vesta have similar masses (Standish *et al.* 1995), sizes, and shapes, so if Vesta's regolith is mature (by asteroid standards) and if both asteroids have experienced the same impactor flux, then differences in decimeter-scale surface roughness between Pallas and Vesta must be due to differences in material strength. Since weak carbonaceous material is more readily comminuted than is basaltic material, Pallas would be expected to have a finer-grained regolith, other things being equal (Langevin and Maurette 1981). This interpretation is supported by a larger mean value of μ_C for S-class MBAs than for C-class MBAs (OCS85). On the other hand, Vesta's circular polarization ratio is higher than those of most radar-detected S-class MBSs (OCS85), all of which are much smaller than Vesta. This is contrary to theoretical predictions (Cintala *et al.* 1978), unless Vesta is significantly stronger than S-class asteroids.

The above considerations suggest the possibility that Vesta's regolith is relatively immature. The lifetime against collisional disruption of a meter-sized rock on an asteroid's surface has been estimated to be $\sim 10^7$ years (Belton *et al.* 1994), and somewhat longer if overturning of the regolith is taken into account (Lee *et al.* 1996). However, this does not limit the age of Vesta's surface, since rocks in the centimeter-to-meter size range can be produced by the breakup of larger blocks. Lee *et al.* (1996) estimate that blocks up to ~1 km in size could be produced during the formation of the large impact basins inferred to be present on Vesta's surface[3] (Drummond *et al.* 1988, Gaffey 1995, Zellner and Storrs 1995, Thomas *et al.* 1995). The progressive breakup of meter-to-kilometer blocks could provide a continuing source of decimeter-scale roughness for billions of years.

Since Vesta's gravity should be sufficiently strong to prevent a uniform, global distribution of ejecta for a given impact (Housen *et al.* 1979), the 13-cm-wavelength circular polarization ratio might exhibit spatial variations if the largest impacts contribute a significant fraction of the total decimeter-scale roughness. Currently recognized impact features are confined to a single hemisphere of Vesta (Gaffey 1995), so even rotationally resolved, disk-integrated measurements might be sufficient to detect variations in surface roughness. Existing data hint at such a possibility (see Section 5) but lack sufficient SNR to make a definitive statement.

7. FUTURE OBSERVATIONS

Prospects for future radar observations of Ceres, Pallas, and Vesta are excellent. Major improvements to the Arecibo telescope currently underway are expected to provide a ~20-fold increase in radar sensitivity (Campbell *et al.* 1994). Table VIII lists OC SNR predictions for selected opportunities between 1997 and 2007 to observe our three targets. Experiments spanning several days for each target should provide sufficient rotation phase coverage and SNR to produce OC radar albedo maps.

[3] It is possible to detect such features on Vesta because the asteroid has been resurfaced with a basaltic layer. We do not have similar means to determine if Ceres and Pallas have experienced similar impacts on the same time scale.

TABLE VIII
Future Radar Opportunities

Target	(1) Current Total SNR	(2) Future SNR per day	(3) δ	(4) Year
Ceres	21	110	+6	1998
		190	0	2000
		140	+7	2004
		100	+3	2007
Pallas	52	50	+12	2000
		270	−48	2005
Vesta	13	50	−9	1997
		150	+25	1999
		110	+7	2001
		220	+17	2003
		120	+21	2006

(1) The OC SNR from the best Arecibo experiment to date (see Table V).
(2) Predicted OC SNR per day for nominal parameters of the upgraded Arecibo radar. For each prediction we assume a radar cross section given by the product of the target's radar albedo (Table VII) and the projected area of a sphere with the target's radiometric diameter. We believe these predictions to be reliable within ~30%.
(3) Predicted subradar latitude during each apparition based on the pole directions listed in Table II (for Pallas we use the prograde model).
(4) Selected opportunities between 1997 and 2007. The Arecibo upgrade is expected to be complete by late-1996.

Arecibo echoes from Ceres, Pallas, and Vesta are "overspread,"[4] precluding complete and unambiguous delay-Doppler imaging with a repetitive waveform (Ostro 1993); however, techniques are available to overcome this limitation. As a target rotates, the Doppler trajectory of a (hypothetical) radar brightness feature depends on its location on the surface. The rotational evolution of a Doppler-only spectrum may thus be used to produce reflectivity maps using the technique described by Hudson (1991) and Hudson and Ostro (1990) and applied to Mars (Harmon *et al.* 1992a) and the icy Galilean satellites (Ostro *et al.* 1992). Alternatively, the nonrepetitive, "random-code" delay-Doppler technique described by Sulzer (1986, 1989) and applied to Mars (Harmon *et al.* 1992b) redistributes delay-aliased echo power into additive white noise, which avoids aliasing in delay or Doppler at the expense of reduced SNR.

Both of the above techniques are still subject to north–south aliasing, so mapping accuracy will depend on observing geometry and orientational coverage. Predicted subradar latitudes are listed in Table VIII for each radar opportunity. Observations of Ceres are limited to subradar latitudes within a few degrees of equatorial, which will not provide sufficient geometric leverage to resolve the north–south ambiguity, but even a north–south aliased map could still prove useful. Radar opportunities for Pallas and Vesta occur during more favorable geometries, and combining data with two or more distinct observing geometries can yield significant improvements (see, e.g., Hudson and Ostro 1990). With Vesta's high circular polarization ratio, future radar observations should yield both albedo and polarization maps.

[4] The product of the echo's dispersions in time delay and Doppler frequency is greater than unity.

ACKNOWLEDGMENTS

We thank the staff of the Arecibo Observatory and the Goldstone Radio Astronomy/Radar Group for assistance with the observations. Part of this research was conducted at the Jet Propulsion Laboratory, California Institute of Technology, under contract with the National Aeronautics and Space Administration (NASA). Work at Washington State University and at the Center for Astrophysics was supported in part by NASA. D.L.M. is grateful for support from the National Research Council. The Arecibo Observatory is part of the National Astronomy and Ionosphere Center, which is operated by Cornell University under a cooperative agreement with the National Science Foundation and with support from NASA.

REFERENCES

Belton, M. J. S., C. R. Chapman, J. Veverka, K. P. Klaasen, A. Harch, R. Greeley, R. Greenberg, J. W. Head III, A. McEwen, D. Morrison, P. C. Thomas, M. E. Davies, M. H. Carr, G. Neukum, F. P. Fanale, D. R. Davis, C. Anger, P. J. Gierasch, A. P. Ingersoll, and C. B. Pilcher 1994. First images of asteroid 243 Ida. *Science* **265,** 1543–1547.

Binzel, R. P. 1984. 2 Pallas: 1982 and 1983 lightcurves and a new pole solution. *Icarus* **59,** 456–461.

Binzel, R. P., and S. Xu 1993. Chips off of asteroid 4 Vesta: Evidence for the parent body of basaltic achondrite meteorites. *Science* **260,** 186–191.

Burchi, R., V. D'Ambrosio, P. Tempesti, and N. Lanciano 1985. Rotational properties of asteroids 2, 12, 80, 145 and 354 obtained by photoelectric photometry. *Astron. Astrophys. Suppl.* **60,** 9–15.

Burchi, R., and L. Milano 1983. 2 Pallas pole revisited. *Moon Planets* **28,** 17–21.

Butler, B. J., D. O. Muhleman, and M. A. Slade 1993. Mercury: Full-disk radar images and the detection and stability of ice at the North Pole. *J. Geophys. Res.* **98**(E8), 15003–15023.

Campbell, D. B., G. J. Black, and S. J. Ostro 1994. Asteroids and comets: Future imaging opportunities with Earth-based radar systems. *Bull. Am. Astron. Soc.* **26,** 1167.

Carrier, W. D., G. R. Olhoeft, and W. Mendell 1991. Physical properties of the lunar surface. In *Lunar Sourcebook* (G. Heiken, D. Vaniman, and B. M. French, Eds.), pp. 475–594. Cambridge Univ. Press, New York/London.

Cellino, A., V. Zappalà, M. Dimartino, P. Farinella, and P. Paolicchi 1987. Flattening, pole, and albedo features of 4 Vesta from photometric data. *Icarus* **70,** 546–565.

Cintala, M. J., J. W. Head, and J. Veverka 1978. Characteristics of the cratering process on small satellites and asteroids. *Proc. Lunar Planet. Sci. Conf. 9th,* 3803–3830.

Davis, D. R., C. R. Chapman, S. J. Weidenschilling, and R. Greenberg 1985. Collisional history of asteroids: Evidence from Vesta and the Hirayama families. *Icarus* **62,** 30–53.

Dollfus, A., M. Wolff, J. E. Geake, D. F. Lupishko, and L. M. Dougherty 1989. Photopolarimetry of asteroids. In *Asteroids II* (R. P. Binzel, T. Gehrels, and M. S. Matthews, Eds.), pp. 594–616. Univ. of Arizona Press, Tucson.

Drummond, J. D., and W. J. Cocke 1989. Triaxial ellipsoid dimensions and rotational pole of 2 Pallas from two stellar occultations. *Icarus* **78,** 323–329.

Drummond, J., A. Eckart, and E. K. Hege 1988. Speckle interferometry of asteroids IV: Reconstructed images of 4 Vesta. *Icarus* **73,** 1–14.

Drummond, J. D., and E. K. Hege 1988. Speckle interferometry of asteroids. In *Asteroids II* (R. P. Binzel, T. Gehrels, and M. S. Matthews, Eds.), pp. 171–191. Univ. of Arizona Press, Tucson.

Dunham, D. W., J. B. Dunham, R. P. Binzel, D. S. Evans, M. Freuh, G. W. Henry, M. F. A'Hearn, R. G. Schnurr, R. Betts, H. Haynes, R. Orcutt, E. Bowell, L. H. Wasserman, R. A. Nye, H. L. Giclas, C. R. Chapman, R. D. Dietz, C. Moncivais, W. T. Douglass, D. C. Parker, J. D. Beish, J. O. Martin, D. R. Monger, W. B. Hubbard, H. J. Reitsema, A. R. Klemola, P. D. Lee, B. R. McNamara, P. D. Maley, P. Manley, N. L. Markworth, R. Nolthenius, T. D. Oswalt, J. A. Smith, E. F. Strother, H. R. Povenmire, R. D. Purrington, C. Trenary, G. H. Schneider, W. J. Schuster, M. A. Moreno, J. Guichard, G. R. Sanchez, G. E. Taylor, A. R. Upgren, T. C. Van Flandern 1990. The size and shape of (2) Pallas from the 1983 occultation of 1 Vulpeculae. *Astron. J.* **99,** 1636–1662.

Evans, J. V., and T. Hagfors 1966. Study of radio echoes from the Moon at 23 centimeters wavelength. *J. Geophys. Res.* **71,** 4871–4889.

Feierberg, M. A., L. A. Lebofsky, and H. A. Larson 1981. Spectroscopic evidence for aqueous alteration products on the surfaces of low-albedo asteroids. *Geochim. Cosmochim. Acta* **45,** 971–981.

Gaffey, M. J. 1996. Surface lithologic heterogeneity of asteroid 4 Vesta. Submitted to *Icarus*.

Garvin, J. B., J. W. Head, G. H. Pettengill, and S. H. Zisk 1985. Venus global radar reflectivity and correlations with elevation. *J. Geophys. Res.* **90,** 6859–6871.

Glass, B. T. 1982. *Introduction to Planetary Geology,* Cambridge Univ. Press, Cambridge.

Hagfors, T. 1967. A study of the depolarization of lunar radar echoes. *Radio Sci.* **2,** 445–465.

Hainaut, O. 1995. Hubble shoots Vesta. *Sky Telescope,* April 1995, pp. 14–15.

Harmon, J. K., and S. J. Ostro 1985. Mars: Dual-polarization radar observations with extended coverage. *Icarus* **62,** 110–128.

Harmon, J. K., M. A. Slade, and R. S. Hudson 1992a. Mars radar scattering: Arecibo/Goldstone results at 12.6- and 3.5-cm wavelengths. *Icarus* **98,** 240–253.

Harmon, J. K., M. P. Sulzer, P. J. Perillat, and J. F. Chandler 1992b. Mars radar mapping: Strong backscatter from the Elysium basin and outflow channel. *Icarus* **95,** 153–156.

Housen, K. R., L. L. Wilkening, C. R. Chapman, and R. J. Greenberg 1979. Regolith development and evolution on asteroids and the Moon. In *Asteroids* (T. Gehrels, Ed.), pp. 601–627. Univ. of Arizona Press, Tucson.

Hudson, R. S. 1991. *Radar Imaging for Aircarft Identification and Planetary Astronomy.* Ph.D. Dissertation, California Institute of Technology.

Hudson, R. S. 1993. Three-dimensional reconstruction of asteroids from radar observations. *Remote Sensing Rev.* **8,** 195–203.

Hudson, R. S., and S. J. Ostro 1990. Doppler radar imaging of spherical planetary surfaces. *J. Geophys. Res.* **95** (B7), 10947–10963.

Hudson, R. S., and S. J. Ostro 1994. Shape of asteroid 4769 Castalia (1989 PB) from inversion of radar images. *Science* **263,** 940–943.

Hudson, R. S., and S. J. Ostro 1995. Shape and non-principal axis spin state of asteroid 4179 Toutatis. *Science* **270,** 84–86.

Jones, T. D., L. A. Lebofsky, J. S. Lewis, and M. S. Marley 1990. The composition and origin of the C, P, and D asteroids: Water as a tracer of thermal evolution in the outer belt. *Icarus* **88,** 172–192.

Jurgens, R. F., and R. M. Goldstein 1976. Radar observations at 3.5 and 12.6 cm wavelength of asteroid 433 Eros. *Icarus* **28,** 1–15.

Lagerkvist, C.-I., M. A. Barucci, M. T. Capria, M. Fulchignoni, L. Guerriero, E. Perozzi, and V. Zappalà 1987. *Asteroid Photometric Catalog.* Consiglio Nazionale delle Richerche, Rome.

Lagerkvist, C.-I., M. A. Barucci, M. T. Capria, M. Fulchignoni, P. Magnusson, and V. Zappalà 1988. *Asteroid Photometric Catalog,* First Update. Consiglio Nazionale delle Richerche, Rome.

Lagerkvist, C.-I., A. W. Harris, and V. Zappalà 1989. Asteroid lightcurve parameters. In *Asteroids II* (R. P. Binzel, T. Gehrels, and M. S. Matthews, Eds.), pp. 1162–1179. Univ. of Arizona Press, Tucson.

Lambert, J. V. 1985. *Occultation and Lightcurve Analysis: The Figure of 2 Pallas*. Ph.D. thesis, New Mexico State University.

Langevin, Y., and M. Maurette 1981. Grain size and maturity in lunar and asteroidal regoliths. *Lunar Planet. Sci.* **12,** 595 (abstract).

Larson, H. P., M. A. Feierberg, and L. A. Lebofsky 1983. The composition of asteroid 2 Pallas and its relation to primitive meteorites. *Icarus* **56,** 398–408.

Lebofsky, L. A., M. A. Feierberg, A. T. Tokunaga, H. P. Larson, and J. R. Johnson 1981. The 1.7- to 4.2-μm spectrum of asteroid 1 Ceres: Evidence for structural water in clay minerals. *Icarus* **48,** 453–459.

Lee, P., J. Veverka, P. C. Thomas, P. Helfenstein, M. J. S. Belton, C. R. Chapman, R. Greeley, R. T. Pappalardo, R. Sullivan, and J. W. Head 1996. Ejecta blocks on 243 Ida and on other asteroids. *Icarus* **120,** 87–105.

Magnusson, P. 1986. Distribution of spin axes and senses of rotation for 20 large asteroids. *Icarus* **68,** 1–39.

McCarthy, D. W., Jr., J. D. Freeman, and J. D. Drummond 1994. High resolution images of Vesta at 1.65 μm. *Icarus* **108,** 285–297.

McCollom, T. M., and B. M. Jakosky 1993. Interpretation of planetary radar observations: The relationship between actual and inferred slope distributions. *J. Geophys. Res.* **98,** (No. E1), 1173–1184.

McKay, D. S., T. D. Swindle, and R. Greenberg 1989. Asteroidal regoliths: What we do not know. In *Asteroids II* (R. P. Binzel, T. Gehrels, and M. S. Matthews, Eds.), pp. 617–642. Univ. of Arizona Press, Tucson.

Millis, R. L., L. H. Wasserman, O. G. Franz, R. A. Nye, R. C. Oliver, T. J. Kreidl, S. E. Jones, W. Hubbard, L. Lebofsky, R. Goff, R. Marcialis, M. Sykes, J. Freckler, D. Hunten, B. Zellner, H. Reitsema, G. Schneider, E. Dunham, J. Klavetter, K. Meech, T. Oswalt, J. Rafert, E. Strother, J. Smith, H. Povenmire, B. Jones, D. Kornbluh, L. Reed, K. Izor, M. F. A'Hearn, R. Schnurr, W. Osborn, D. Parker, W. T. Douglas, J. D. Beish, A. R. Klemola, M. Rios, A. Sanchez, J. Piironen, M. Mooney, R. S. Ireland, and D. Leibow 1987. The size, shape, density, and albedo of Ceres from its occultation of BD + 8°471. *Icarus* **72,** 507–518.

Mitchell, D. L., S. J. Ostro, K. D. Rosema, R. S. Hudson, D. C. Campbell, J. F. Chandler, and I. I. Shapiro 1995. Radar observations of asteroids 7 Iris, 9 Metis, 12 Victoria, 216 Kleopatra, and 654 Zelinda. *Icarus* **118,** 105–131.

Ostro, S. J. 1987. Physical properties of asteroids from radar observations. In *Evolution of the Small Bodies of the Solar System* (M. Fulchignoni and L. Kresák, Eds.), pp. 131–146. Elsevier Science, Amsterdam.

Ostro, S. J. 1993. Planetary radar astronomy. *Rev. Mod Phys.* **65** (No. 4), 1235–1279.

Ostro, S. J., D. B. Campbell, J. F. Chandler, A. A. Hine, R. S. Hudson, K. D. Rosema, and I. I. Shapiro 1991. Asteroid 1986 DA: Radar evidence for a metallic composition. *Science* **252,** 1399–1404.

Ostro, S. J., D. B. Campbell, G. H. Pettengill, and I. I. Shapiro 1980. Radar detection of Vesta. *Icarus* **43,** 169–171.

Ostro, S. J., D. B. Campbell, and I. I. Shapiro 1983. Radar observations of asteroid 1685 Toro. *Astron. J.* **88,** 565–576.

Ostro, S. J., D. B. Campbell, and I. I. Shapiro 1985. Mainbelt asteroids: Dual-polarization radar observations. *Science* **229,** 442–446.

Ostro, S. J., A. W. Harris, D. B. Campbell, I. I. Shapiro, and J. W. Young 1984. Radar and photoelectric observations of asteroid 2100 Ra-Shalom. *Icarus* **60,** 391–403.

Ostro, S. J., D. B. Campbell, R. A. Simpson, R. S. Hudson, J. F. Chandler, K. D. Rosema, I. I. Shapiro, E. M. Standish, R. Winkler, D. K. Yeomans, R. Vélez, and R. M. Goldstein 1992. Europa, Ganymede, and Callisto: New radar results from Arecibo and Goldstone. *J. Geophys. Res.* **97,** 18227–18244.

Ostro, S. J., J. F. Chandler, A. A. Hine, K. D. Rosema, I. I. Shapiro, and D. K. Yeomans 1990. Radar images of asteroid 1989 PB. *Science* **248,** 1523–1528.

Ostro, S. J., G. H. Pettengill, I. I. Shapiro, D. B. Campbell, and R. R. Green 1979. Radar observations of asteroid 1 Ceres. *Icarus* **40,** 355–358.

Parker, M. N. 1973. *Radio-wave Scattering from Rough Surfaces and the Estimation of Surface Shape.* Ph.D. dissertation, Stanford University, Stanford, CA.

Pettengill, G. H. 1978. Physical properties of the planets and satellites from radar observations. *Annu. Rev. Astron. Astrophys.* **16,** 265–292.

Redman, R. O., P. A. Feldman, H. E. Matthews, I. Halliday, and F. Creutzberg 1992. Millimeter and submillimeter observations of the asteroid 4 Vesta. *Astron. J.* **104,** 405–411.

Saint Pé, O., M. Combes, and F. Rigaut 1993. Ceres surface properties by high-resolution imaging from Earth. *Icarus* **105,** 271–281.

Schroll, A., H. F. Haupt, and H. M. Maitzen 1976. Rotation and photometric characteristics of Pallas. *Icarus* **27,** 147–156.

Shepard, M. K., R. A. Brackett, and R. E. Arvidson 1995. Self-affine (fractal) topography: Surface parameterization and radar scattering. *J. Geophys. Res.* **100** (No. E6), 11709–11718.

Simpson, R. A., and G. L. Tyler 1982. Radar scattering laws for the lunar surface. *IEEE Trans. Antennas Propag.* **AP-30** (No. 3), 438–449.

Spencer, J. R., L. A. Lebofsky, and M. V. Sykes 1989. Systematic biases in radiometric diameter determinations. *Icarus* **78,** 337–354.

Standish, E. M., X. X. Newhall, J. G. Williams, and W. M. Folkner 1995. *JPL Planetary and Lunar Ephemerides.* DE403/LE403 (JPL IOM 314.10–127).

Sulzer, M. P. 1986. A radar technique for high range resolution incoherent scatter autocorrelation function measurements utilizing the full average power of klystron radars. *Radio Sci.* **21,** 1033–1040.

Sulzer, M. P. 1989. Recent incoherent scatter techniques. *Adv. Space Res.* **9,** 153–162.

Tedesco, E., R. C. Taylor, J. Drummond, D. Harwood, I. Nikoloff, F. Scaltriti, H. J. Schober, and V. Zappalà 1983. Worldwide photometry and lightcurve observations of 1 Ceres during the 1975–1976 apparition. *Icarus* **54,** 23–29.

Tholen, D. J. 1989. Asteroid taxonomic classifications. In *Asteroids II* (R. P. Binzel, T. Gehrels, and M. S. Matthews, Eds.), pp. 1139–1150. Univ. of Arizona Press, Tucson.

Thomas, P. C., R. P. Binzel, M. J. Gaffey, A. Storrs, E. N. Wells, and B. Zellner 1995. Vesta: HST observations of shape, spin pole, and surface features. *Bull. Am. Astron. Soc.* **27**.

Tiuri, M. E. 1964. Radio astronomy receivers. *IEEE Trans. Antennas Propag.* **AP-12,** 930–938.

Tsvetkova, V. S., V. N. Dudinov, S. B. Novikov, Ye. A. Pluzhnik, Yu. G. Shkuratov, V. G. Vakulik, and A. P. Zheleznyak 1991. Shape and size of asteroid 4 Vesta: Speckle interferometry and polarimetry. *Icarus* **92,** 342–349.

Tyler, G. L. 1979. Comparison of quasi-specular radar scatter from the Moon with surface parameters obtained from images. *Icarus* **37,** 29–45.

Wasserman, L. H., R. L. Millis, O. G. Franz, E. Bowell, N. M. White, H. L. Giclas, L. J. Martin, J. L. Elliot, E. Dunham, D. Mink, R. Baron, R. K. Honeycutt, A. A. Henden, J. E. Kephart, M. F. A'Hearn, H. J. Reitsema, R. Radick, and G. E. Taylor 1979. The diameter of Pallas from its occultation of SAO 85009. *Astron. J.* **84,** 259–268.

Zappalà, V., and Z. Knežević 1984. Rotation axes of asteroids: Results for 14 objects. *Icarus* **59,** 436–455.

Zellner, B., and A. Storrs 1995. Hubble shoots Vesta. *Sky Telescope,* April 1995, pp. 14–15.

Zisk, S. H., G. H. Pettengill, and G. W. Catuna 1974. High-resolution radar maps of the lunar surface at 3.8-cm wavelength. *Moon* **10,** 17–50.